Finite Element Analysis and Scale-bridging Calculations of Graphene Crinkle

By

Xincheng Wang

B.Eng., Lanzhou University of Technology, 2019

Thesis

Submitted in partial fulfillment of the requirements for
the Degree of Master of Science in the School of Engineering at Brown University

PROVIDENCE, RHODE ISLAND

March 2021

This thesis by Xincheng Wang is accepted in its present form by the School of Engineering as satisfying the thesis requirements for the degree of Master of Science

Date_____ Signature: _____

Dr. Kyung-Suk Kim, Advisor

Approved by the Graduate Council

Date_____ Signature: _____

Dr. Andrew G. Campbell, Dean of the Graduate School

Acknowledgments

I am deeply grateful for the patient guidance, kind support, and continual encouragement of Professor Kim throughout this thesis project and my Master's study. His insight and knowledge of mechanics, physics, and many other subjects I can only hope to emulate. Professor Kim taught me how to do research, always be critical thinking, and ask good questions during the study.

I would also express my sincere gratitude to Professor Bower and Professor Chason for their encouragement and guidance during my first year of summer research.

I thank my lab member Hanxun Jin and Siyuan Song, who spend a lot of time helping me with my simulation and experiments. I would also thank my friends at Brown and make my life enjoyable, particularly Xiaozhou Fan, Sucheng Zheng, Duo Wen, Boyi Yu.

Finally, I would like to thank my parents for their unconditional love and support during my pursuit of an M.Sc. degree in the United States.

Table of Contents

Table of Figures

Table of Tables

ABSTRACT

Over a decade, it is known that nanopore sequencing of DNA or RNA requires substantial reduction of entropic noise in the nanopore reading process. Recently, a properly aligned flexoelectric graphene crinkle near the nanopore is proposed to reduce the noise. To this end, a multi-layer graphene (MLG) with a nanopore at its center is suspended over an hourglass-shaped through-thickness hole in a stretched silicon-nitride thin layer. Then, the stretching is released to buckle the MLG film to create a desirable flexoelectric graphene crinkle. In this study, hybrid analyses of multi-stage finite element simulations and a scale-bridging analysis are made to characterize and control the crinkle configuration. In the multi-stage finite element simulations, a homogeneous thin elastic film instead of an MLG is employed to approximately evaluate the displacements along the edges of the hourglass-shaped hole. Then, the displacement is used to obtain MLG's surface slopes and curvature along the crinkle ridge, utilizing the relationship between the slope and the curvature of a quantum-flexoelectric crinkle. The results show that proper MLG crinkles can be created and controlled by simple bending and unbending of the substrate to smoothly feed the DNA or RNA into the nanopore without breaking the device.

Chapter 1: Introduction

1.1 Nanotechnology and nanostructured materials

Nowadays, nanotechnology has advanced to produce various 2D functional materials and 3D hierarchical nanostructures, such as graphene, hexagonal boron nitride, nanotube, and graphene aerogels. These advanced nanomaterials have widespread applications in flexible electronics [1], artificial skins [2], biomedical labeling, and brain science. Graphene is well-known for its 2D configuration and excellent scalability, and it can be scaled up to build different 3D architected assemblies with different properties. Zhang et al. [4] used a 3D printer to design the three-dimensional topology graphene, such as microstructurally tailored graphene aerogels. Besides, the nanoscale vibration characteristics [5], frictional behavior [6], and instability mechanisms [7] are studied extensively. One of the discoveries is the quantum flexoelectric graphene crinkle [8], which shows unique energetic properties with promising application potential in the future, such as in molecular or nanostructural engineering, and in turn, quantum computing fields.

1.2 *Ruga* mechanics and graphene crinkle

Simultaneously, a hot and fruitful research topic in the solid mechanics community is studying various *ruga* surface morphology from multiple solid surfaces and interfaces. There are many other different corrugated material configurations such as wrinkles, creases, ridges, as shown in the schematic below:

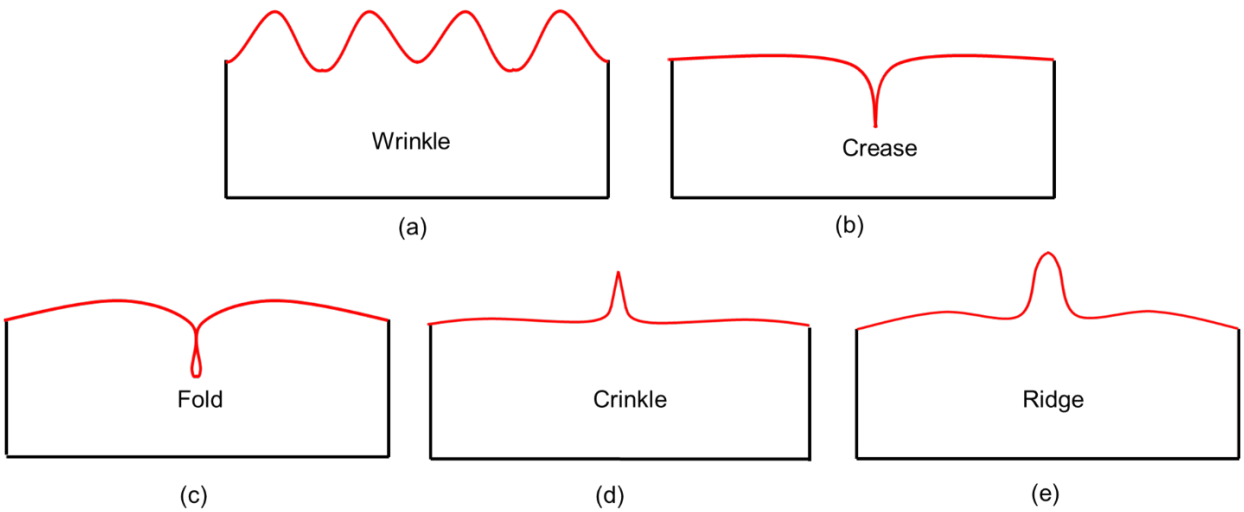

Figure 1.1 Schematics of various *ruga* phases.

The *ruga* surface morphology is universal in biology and engineering materials. For example, the cerebral cortex of humans consists of numerous folded neural tubes and creases, which significantly increases the surface area of neural tissue. The wrinkle is also formed in the surface of the polymer [9], composite materials [10], membranes structures [11], and graphene [12,13]. Morphological characteristics of the *ruga* phases also are found at the nanoscale. Teng et al. [14,15] applied the molecular dynamics method to explore the mechanical behavior and simulate graphene *ruga*. Graphene corrugation was also reported in the experiments. Few layers of graphene exhibit dynamic ripples when suspended [16]. The multi-layer graphene crinkle image was observed in atomic force microscopy [17]. The quantum flexoelectric crinkle [18] leads to the curvature localization on multi-layer graphene. This new subcritical buckling mode produces shallow-kink corrugation in multi-layer graphene. Kothari et al. [19] analyzed the pure mechanical model compared with the electro-mechanical coupling model of multi-layer graphene crinkles. The result shows the curvature focusing bands width is 0.86nm. The high curvature localized in the narrow width leads to the high electrical charge polarization concentration along with the

graphene crinkle, which provides an innovative way to control molecular self-assembly. Li et al. [8] presented the C60 adsorption experiments with natural crinkle on the HOPG surface.

1.3 Graphene-crinkle-assisted next-generation DNA sequencing.

Deoxyribonucleic acid (DNA) is a long-chain polymer made from repeating nucleotides, which plays a critical role in the development, functioning, growth, and reproduction of organisms. It is crucial to decode the biological information behind the DNA chain, and DNA sequencing technology is invented as one of the essential tools in DNA science. The first whole nucleic-acid sequence technique was presented in 1965 [20]. Next, the first-generation DNA sequencing through the protein-coding gene was introduced in 1975 through the protein-coding gene. Maxam et al. [21] applied chemical agents to disassemble the DNA molecule chain to find out the sequence. However, there remain still many limitations for the prototype DNA sequencing, such as the limited read length and slow read speed.

Researchers have been conducting experiments to improve the efficiency and accuracy of DNA sequencing for decades. After the 2000s, researchers [22] have presented a parallel sequencing technique and post-light sequencing [23]. A next-generation single-molecule nanopore DNA sequencing technique with low cost and higher sequencing speeds was introduced [24]. However, the novel solid-state nanopore sequencing technology is not perfect yet because it exhibits a high noise level and lack of atomic-resolution control.

The graphene crinkle nanostructure shows promising prospects in this field by creating ‘molecular brakes.’ The unique electrical properties of graphene crinkles enable graphene to interact with DNA molecules, arranging DNA molecules in electric fields along the paths of the crinkle. Figure (1.2) shown the possible design of the next-generation DNA sequencing with graphene crinkles.

If DNA molecules could be fixed or controlled on a solid surface, the nanopore sequencing technique can be performed well without the concerns of noise and lacking accuracy. It could significantly speed up the new COVID 19 vaccine development and Human Genome Project, for an example.

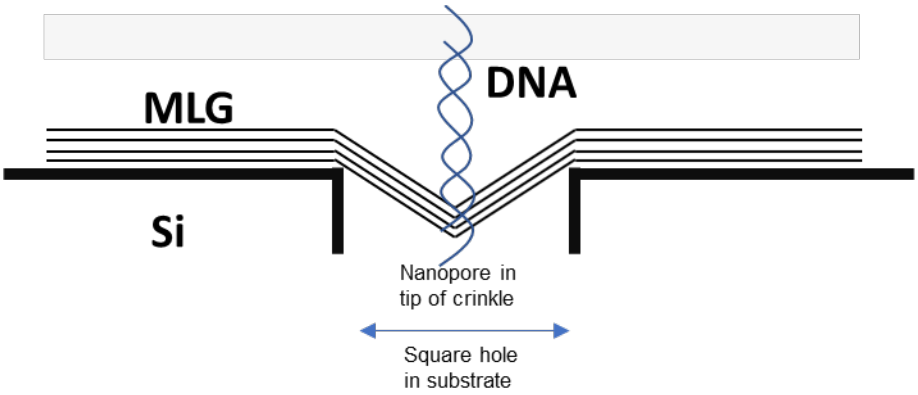

Figure 1.2 A schematic of nanopore DNA sequencing assisted by a graphene crinkle.

In the following chapters of this thesis, we focus on simulating a graphene-crinkle formation process with decomposed finite-element modeling to obtain graphene-emulated-layer (GEL) angle and curvature distributions around the crinkle. Next, we use scale-bridging techiques applied to the decomposed finite-element modeling results to obtain the flexoelectric crinkle angle in the graphene surface. The calculated graphene crinkle configurations and their controllability can be a useful reference for the ongoing DNA adsorption experiments.

Chapter 2: Finite element analysis of graphene crinkle forming process

2.1 Decomposed simulation framework

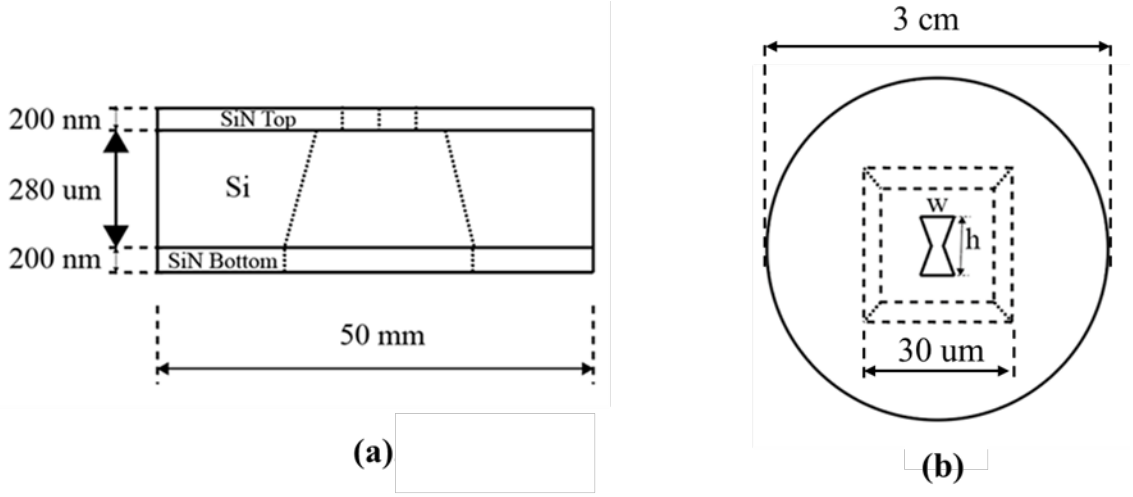

Figure 2.1 Schematics of the sample: (a)(b) left & right side view of the sample with three-layer structure; (b) top view of the sample with a through-thickness hourglass-shaped hole.

The predesigned sample consists of three layers of two different materials. The sample's size and geometry are shown in Figure (2.1), from the top view and the side view separately. In the bottom layer, there is a silicon-nitride (SiN) thin layer with a thickness of 200 nm. Above the SiN thin layer, a silicon (Si)-wafer substrate is constructed as the main body of the sample, with a thickness of 280 μm. Then, another SiN thin layer is attached to the silicon-wafer surface. The sample has a 30 μm × 30 μm square through-thickness hole located in the center of the Si wafer, passing throughout the second and third layer. Figure (2.2) and Figure (2.3) are an SEM image of the square hole and a photographe of the manufacturing process. The square hole in the Si substrate is made to suspend a SiN layer loaded in tension or compression, while the substrate is cut into a 3 mm-diameter TEM sample. Note that the micro-manufacturing process makes the wall of the square hole slightly tilted. Because the graphene crinkle is forming over a small hourglass-shaped

through-thickness hole at the center of the suspended first/top SiN layer, the slight tilt angle in the second Si layer would have a second-order effect on the deformation of the top SiN layer. Thus, we make the square hole wall vertical to the bottom surface in our FEM modeling.

The major significant part of graphene crinkle formation is made by an hourglass-shaped hole in the top silicon-nitride thin-layer. The hourglass-shaped hole has a height of 600 nm and a width of 325 nm, respectively, as seen in Figure (2.4). The shape is carefully conceptualized and designed to make a graded quantum-flexoelectricity graphene-crinkle. The gradually changing distances between two side boundaries make the graphene-crinkle curvature gradually vary along the crikle ridge. The gradual variation of the curvature is the key factor to control adsorption and sliding of a positively charged DNA molecular along the crikle.

Figure 2.2 Manufacturing process and the dimension of a square hole in a silicon substrate.

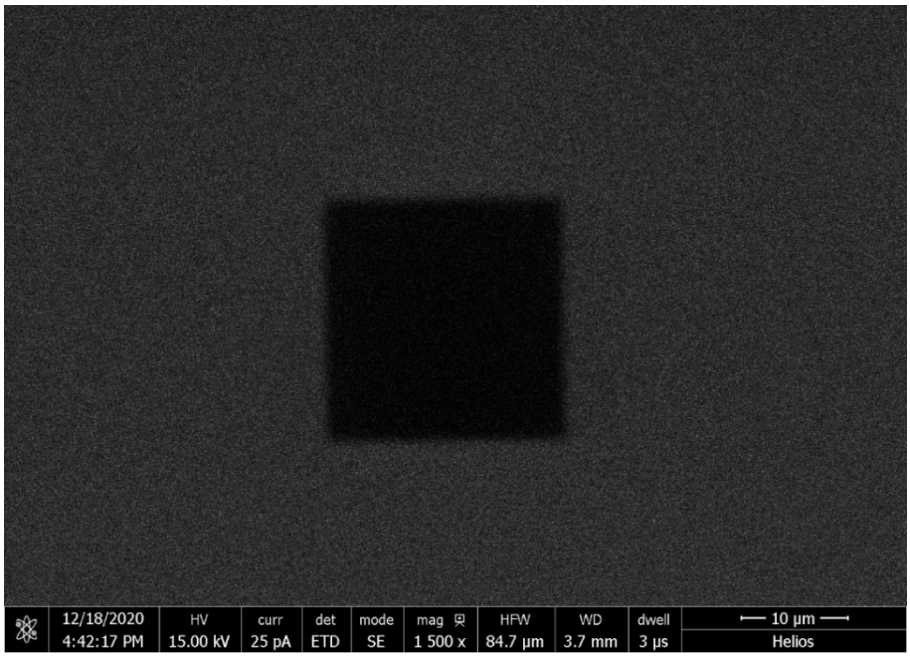

Figure 2.3 SEM image of a through-thickness square hole in the silicon substrate.

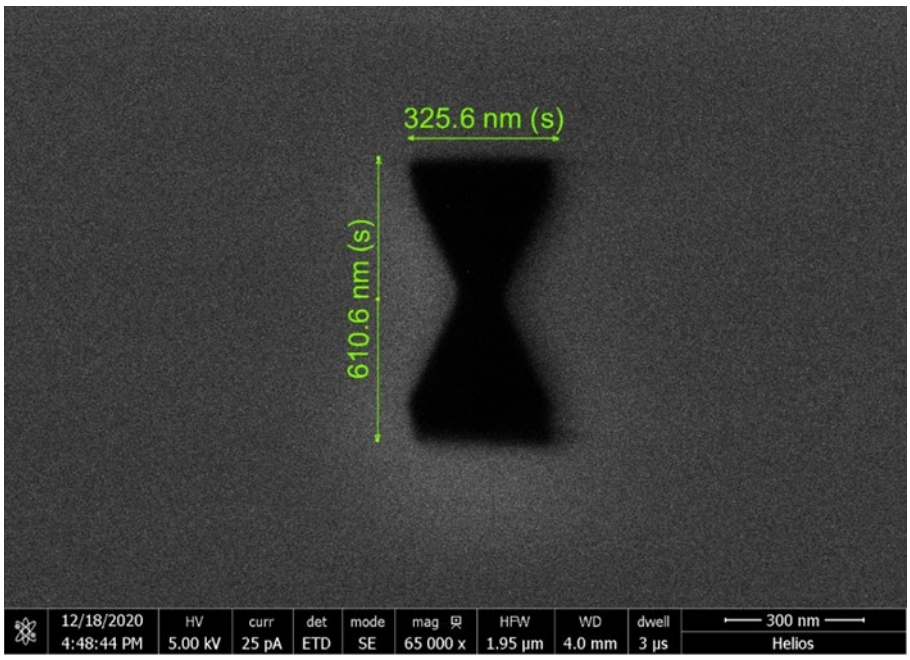

Figure 2.4 SEM image of a hourglass-shaped hole in the silicon-nitride thin layer.

The whole sample is composed of multiscale high-aspect-ratio thin-layer assemblies on a 5-cm-diameter circular plate with a thickness of 280.4 μm. Each thin-layer structure hosts a hole of a characteristic geometry through the layer thickness, over which next-scale thin film is assembled. The aspect ratios of each-scale thin-layer exceed the typical part-modeling ratio for finite element simulations. Therefore, we set up a multi-stage analysis strategy by decomposing the whole analysis into two different-level FEM simulations from the wafer-scale to a microstructure scale and theoretical scale-bridging analysis from the micro-scale to the nano-crinkle scale. For example, the 200nm-thickness silicon-nitride thin layer is thinner than $1/1000^{th}$ the 280um-thickness silicon-wafer substrate, and it is impractical to model the top SiN surface layer with the second Si wafer altogether. In our multi-stage analysis, we emulate the entire experimental procedure. In the experiment procedure, we first bent the silicon wafer with the silicon-nitride thin layer attached. Next, we carefully stick an MLG onto the pre-tensioned SiN thin layer to cover the hourglass-shaped hole while SiN/Si layers are kept bent. After that, we release the sample from the bending apparatus. Consequently, the compressive stress created by the releasing process causes the suspended portion of MLG buckles over the hourglass-shaped hole.

In our study, we simulate the bending deformation of the wafer with FEM to get the displacement filed near the square hole at the center. Then, the displacements adjusted by an impedance-matching factor are used as a part of the boundary conditions for the next-scale FEM analysis of stretching or compressing the SiN layer with an hourglass-shaped hole at the center, as shown in Figure (2.5).

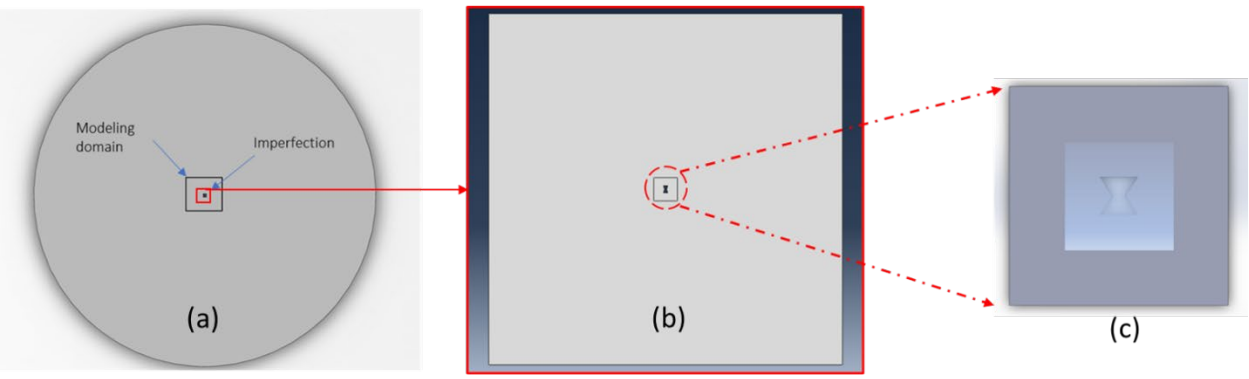

Figure 2.5 Schematics of decomposed simulation objects: (a) silicon-wafer substrate; (b) silicon-nitride thin layer; (c) graphene attached to the silicon nitride over the hourglass-shaped hole.

2.2 Bending analysis of silicon wafer substrate

At a large scale, we first simulate the bending of the silicon wafer substrate. The diameter of the wafer substrate is 5 cm, and the thickness is 280 μm. A 30 μm × 30 μm square hole is located in the substrate center. To reduce the computational cost, we model a limited central region of the Si substrate with a uniform bending-boundary condition, i.e., uniform rotation of the cross-section at the bending boundaries. The simulation domain is set $-150\ \mu m < x < 150\ \mu m$, $-150\ \mu m < y < 150\ \mu m$, $0\ \mu m < z < 280\ \mu m$, excluding the 30 μm × 30 μm square through-thickness hole. We model the silicon wafer linear elastic. Young's modulus is set as 50Gpa, and Poisson's ratio as 0.28. We select the C3D8R element to construct the mesh.

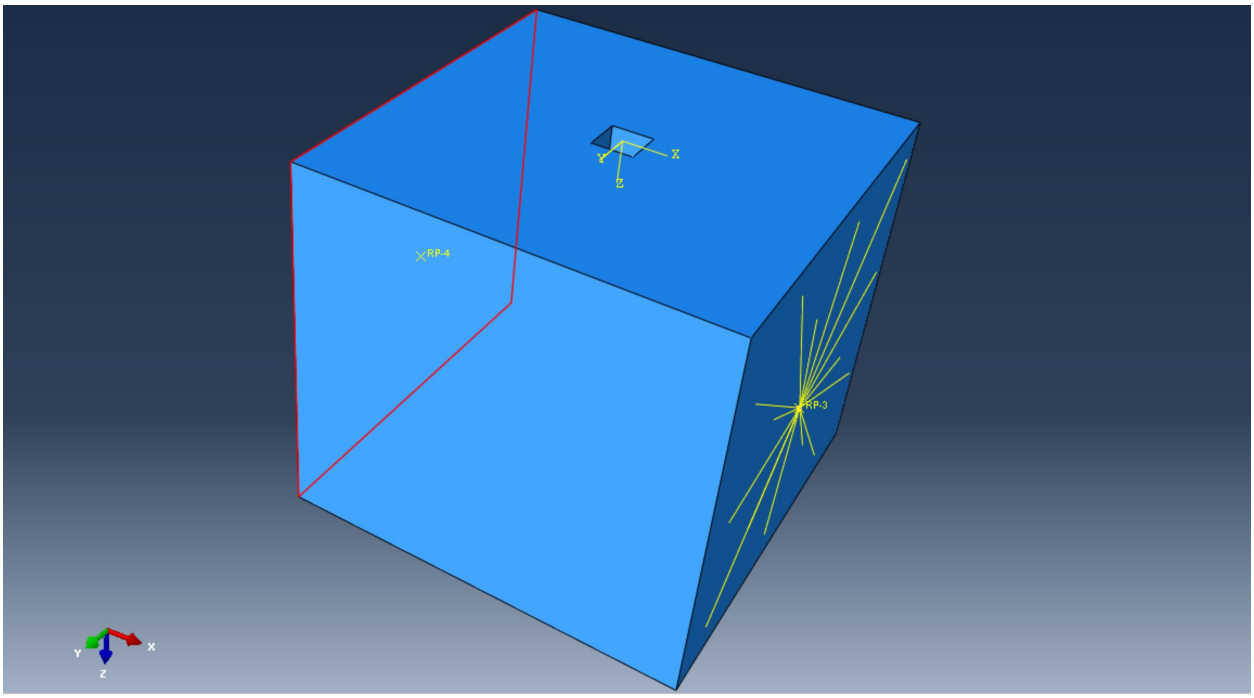

Figure 2.6 Boundary conditions of silicon-substrate bending analysis.

The detailed boundary conditions set as:

Reference point 3: U1 = U2 = UR1 = UR3 = 0, UR2 = 0.05 (radius)

Reference point 4: U1 = U2 = UR1 = UR3 = 0, UR2 = -0.05 (radius)

The 0.05 radius along the global x direction is set to be consistent with the $\pm 3^{\circ}$ bending angle at the two ends. We first apply the boundary conditions to two rigid reference points, and then constraint the reference points to the side surfaces along the $\pm x$ direction. The radial pattern shown in Figure 2.6 is the distributing coupling constraints between the rigid reference point and the one of the side surfaces. By this way the bending curvature can be uniformly apply to the surface without singularity.

Fig (2.7) is the stress distribution of the Si-wafer bending simulation. The upper part of the thick plate is under x-direction tension, while the bottom part of the cubic is under compression. Therefore, the minimum stress appreas in the middle region of our model.

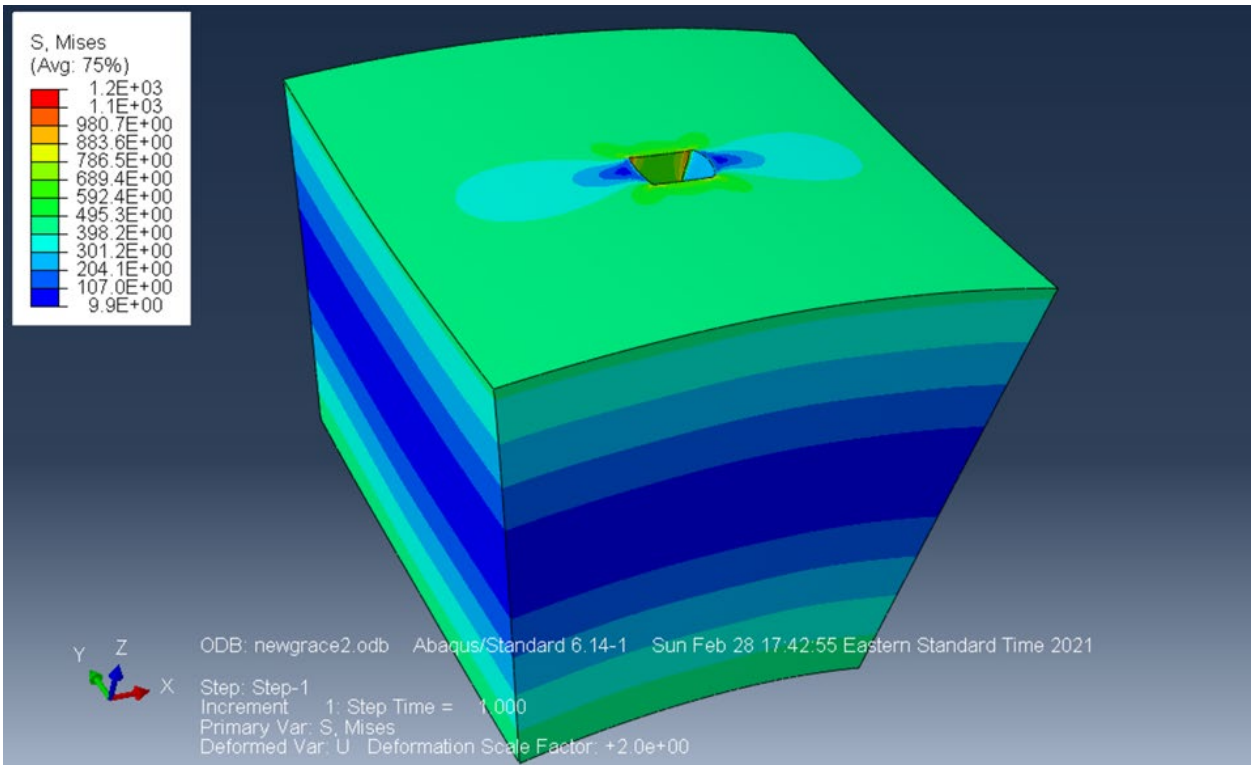

Figure 2.7 Full-field stress distribution of silicon-substrate bending analysis.

Fig (2.8) shows the U1-direction displacement distribution. It can be seen that the absolute U1-displacement distribution is symmetrical along the bending direction. The red-colored part denotes displacement in the positive x-direction, and the blue part indicates the displacement in the negative x-direction. We are most interested in its U1-direction deformation near the square hole since the SiN thin layer is coupled with the square hole surface.

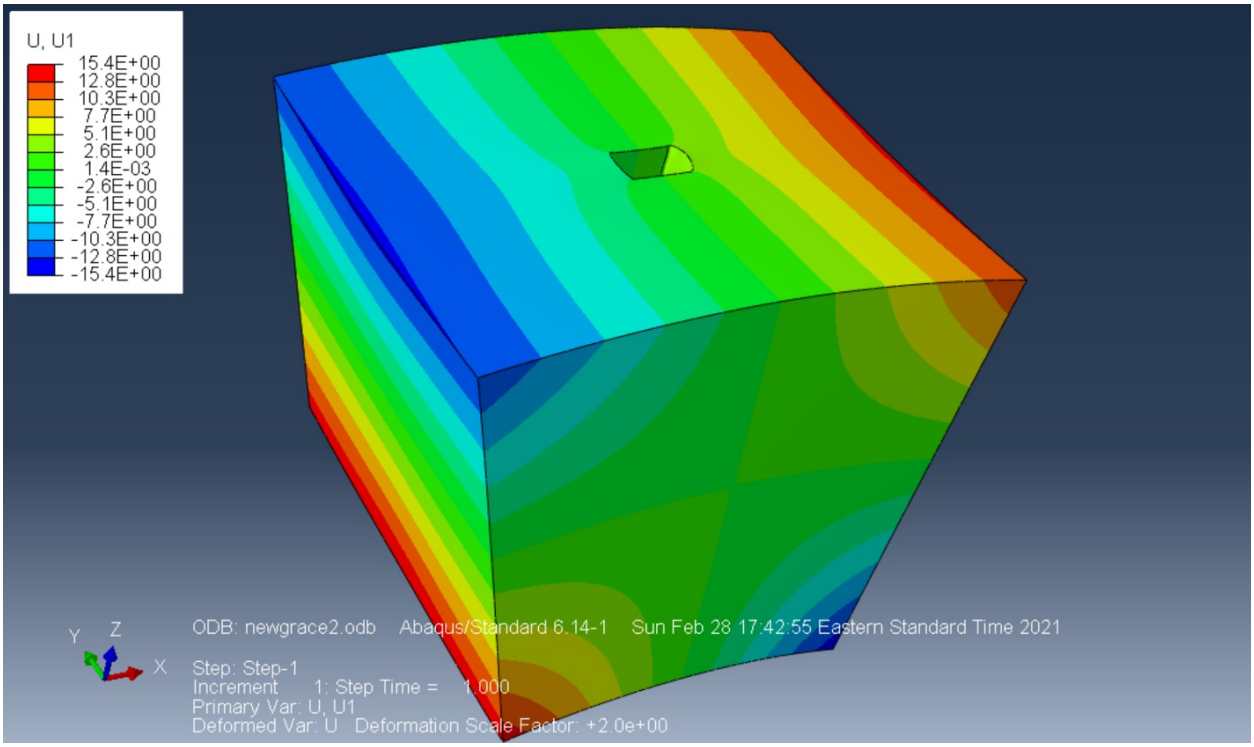

Figure 2.8 Full-field U1 displacement distribution of silicon-substrate bending analysis.

Since the SiN thin layer is closely attached to the top surface of the model, and the deformation near the square hole is continuously transferred to silicon nitride edges. To simplify the model, we assume that the U1 displacement is the dominant deformation field that influences the SiN thin layer.

Thus, the U1 displacement data can be extracted from the square hole imperfection's top edge. Figure (2.9) presents an example of probing nodes and the U1 displacement data. To obtain the continuous displacement field, we use spline interpolation. Shown in Figure (2.10).

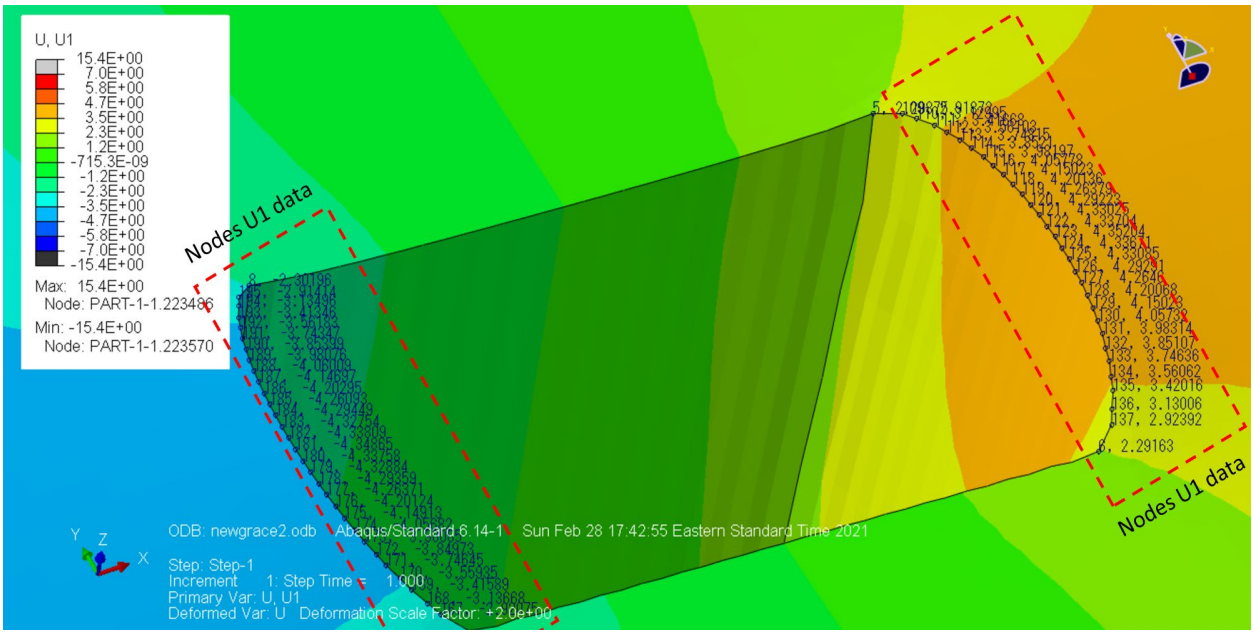

Figure 2.9 Nodal surface displacements near two edges of deformed square hole.

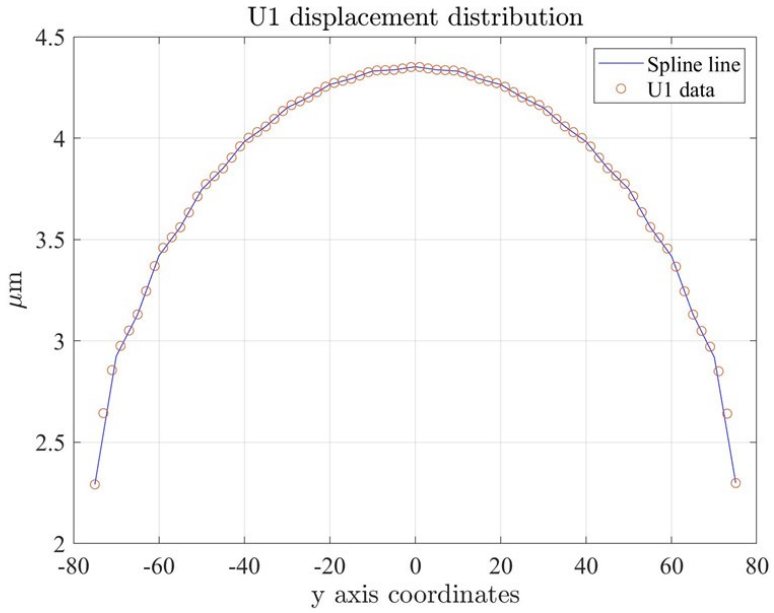

Figure 2.10 Raw nodal-displacement data and splined curve.

An impedance-matching factor is necessary to engineering scale bridging the FE simulations from the wafer-scale to the next microstructure scale. Figure (2.11.a) is the schematics of the current

wafer bending simulation, and Figure (2.11.b) is the schematic of the experiment-emulated simulation.

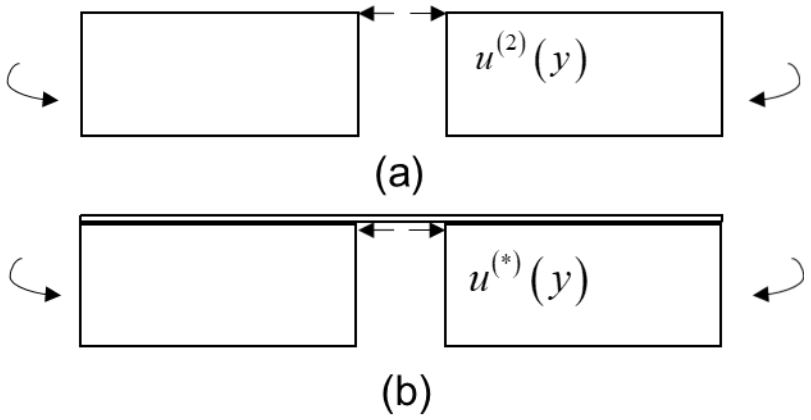

Figure 3.11 Cross-sectional view of sample assembly; (a) a schematic of current Si wafer simulation. (b) a schematic of bending Si wafer coupled with a SiN thin layer.

The x-displacement at the right edges of the square hole in the Si wafer without a SiN thin layer (see Fig. 9) is denoted by $u^{(2)}(y)$, and that with a SiN thin layer $u^{(*)}(y)$. Assuming the structures are linear elastic and the thin layer is compliant, the two displacements are related to each other as

$$u^{(*)}(y) = \alpha(y)u^{(2)}(y) \tag{1}$$

where α is the impedance-matching factor.

If we denote the x-directional tensile force in the layer along the square-hole edge by $f^*(y)$,

$$f^*(y) = \beta_{si}(y)\left(u^{(2)}(y) - u^{(*)}(y)\right) = \beta_L u^{(*)}(y) \tag{2}$$

where $\beta_{si}(y)$ and $\beta_L = Et_{SiN}/l$ are spring constants per unit width of the substrate and the layer for the displacements along the edge. Here, t_{SiN} and l represent the SiN layer thickness and the edge length of the square hole, respectively. For the SiN thin layer of $E = 160\ GPa$, $t_{SiN} =$

0.2 μm, and $l = 30\ \mu m$, the value of β_L becomes $1.06\ GPa$. On the other hand, our FEM analysis provides the average value of $\beta_{si}(y)$ is $326\ GPa$. Equations (1) and (2) are rearranged to have

$$u^{(*)}(y) = \frac{\beta_{si}(y)}{\beta_L + \beta_{si}(y)}\, u^{(2)}(y) = \alpha(y) u^{(2)}(y) \tag{3}$$

Then, when we insert $\beta_L = 1.06\ GPa$ and $\beta_{si}(y) \approx 326\ GPa$, $\alpha(y)$ becomes close to unity. As $\alpha(y) \approx 1$, the FEM displacement results of the Si-wafer-deformation simulation can be directly used as the boundary conditions to the next-stage SiN-layer/graphene-film simulation.

2.3 Stretching analysis of silicon-nitride thin layer

We view the SiN thin layer above the square hole as the thin square sheet. The thin sheet has a size of 30 μm by 30 μm and a thickness of 0.2 μm. We build a 3D solid thin plate with the central hourglass imperfection connect the top-bottom surface. The simulation domain is -150<x<150, -150<y<150, 0<z<1 excluding the 1.75*3 hourglass imperfection. The material properties for silicon nitride set as 160Gpa and 0.3 for Poisson's ratio. The element type keeps the same with the silicon substrate.

The boundary conditions for the silicon nitride tension test set up as follow:

Left side surface: U1 varied along with z axis, U2 = U3 = UR1 = UR2 = UR3 = 0

Right side surface: -U1 varied along with z axis, U2 = U3 = UR1 = UR2 = UR3 = 0

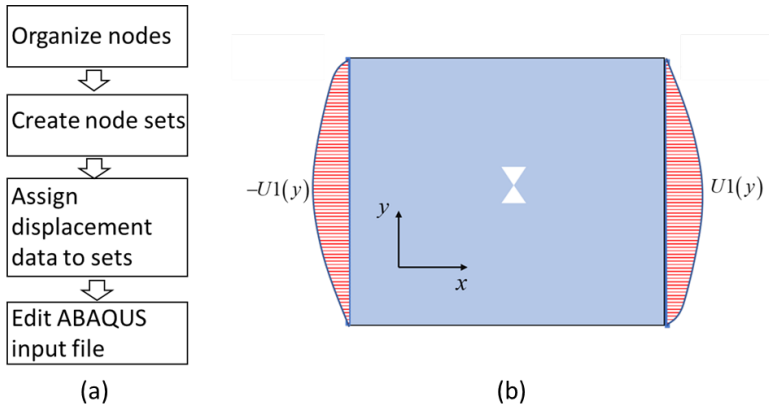

Figure 2.12 Schematics of applying boundary conditions: (a) nodal displacement data implement process; (b) top view of the tension of SiN layer.

Next, we focus on applying the continuous U1 displacement field from silicon wafer to SiN layer. As shown in Figure (2.12), The detailed procedure of applying the U1 displacement is explained as follows. First, we need to build a series of node sets based on their X and Y coordinates. For example, Figure (2.13) shows a detailed view of the nodes and elements in the thin plate edge. A list of nodes shares the same X and Y coordinates, which means they are fixed in the same location from the X-Y plane view. But they have different Z coordinates in the thickness direction.

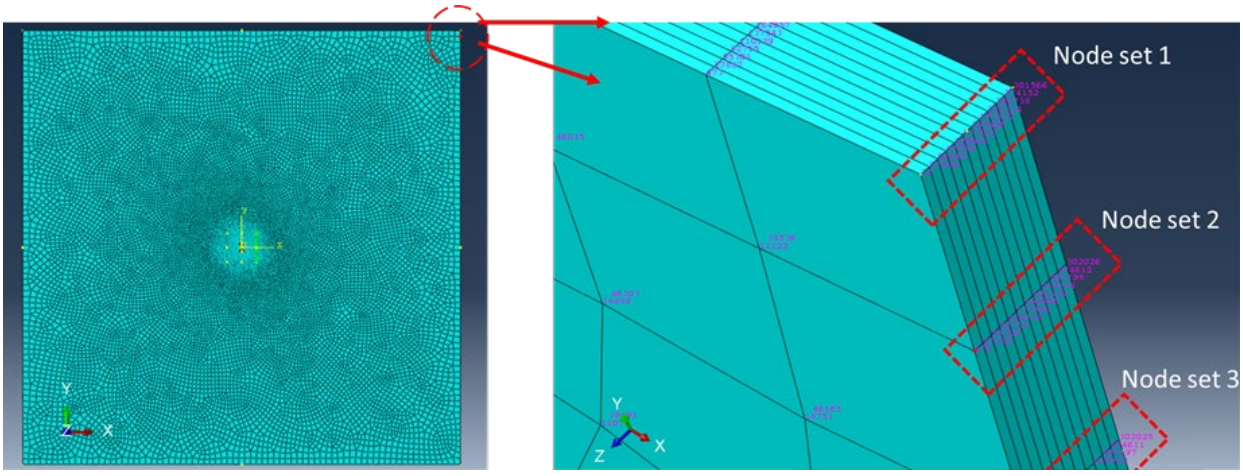

Figure 2.13 Meshing the whole SiN layer: (a)top view of the of the meshed SiN instance; (b) detailed view of node sets.

We recognize these nodes in one set and apply the specified U1 displacement data to the set. The repeating work can be done by writing a MATLAB code to prepare the text file. Last but not least, we replace the node-set definition and boundary condition in the ABAQUS job input file and run the job. Figure (2.14) shows the resulting SiN thin-layer U1 displacement distribution. As we can the displacement field is symmetrical to the hourglass hole, and the maximum U1 displacement for the thin layer is 4.4 μm. The middle part of each edge has larger deformation compared with the four corners.

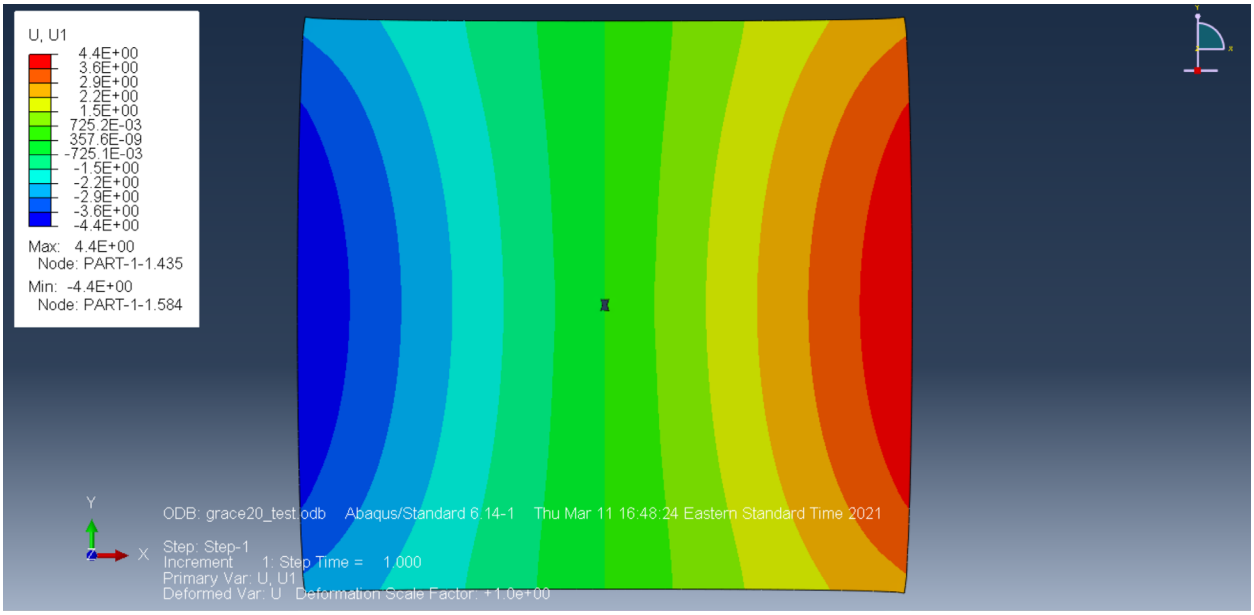

Figure 4.14 Full-field U1 displacement distribution of the silicon nitride of the stretching analysis.

When we zoom in the center of the silicon nitride thin layer, the hourglass hole is deformed along the x-axis direction. Figure (2.15) shows the lateral deformation data in the hourglass hole edge.

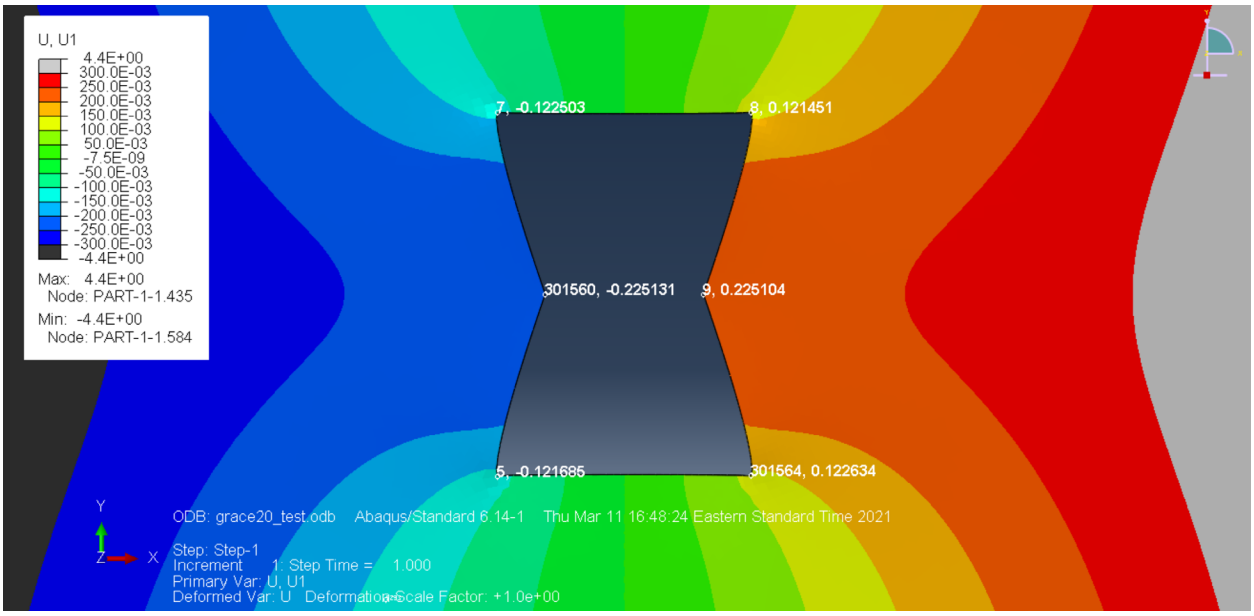

Figure 5.15 Deformed hourglass shape and nodal displacements.

We can see the square hole imperfection from the silicon-wafer bending-simulation results tends to deform as the rectangular shape hole. The square hole top surface is expanding in the direction where the displacement boundary condition is applied (i.e., x direction), while it contracts in the y direction. The hourglass hole has a similar deformation tendency here.

To emulate the experimental compression procedure, we first obtained the deformed hourglass imperfection shape from the tensile test and then created a new silicon nitride model with a deformed hourglass imperfection in the center. Next, we apply the opposite direction displacement boundary conditions to simulate the crinkle forming process. We treat the value of the applied strain rate as one of the parameters to avoid using loading boundary conditions.

In the Si-substrate FEM simulation, the boundary condition for bending deformation is set to be ± 3 degrees in the 300 μm span, which is equivalent to a curvature of 349 m^{-1}. The bending induces approximately ± 3.6 μm on the two opposite edges of the square hole at the center. The FEM simulation results give us response parameter $Q = 0.0103$ $\mu m/(m^{-1})$ of edge displacement

per far-field bending curvature. The Q factor gives the relationship between the boundary displacements at the edges of the square hole and the applied bending curvature of the Si substrate as

$$\pm d_{SiN} = Q\kappa_{Si}\,. \tag{4}$$

where d_{SiN} is the boundary displacement of SiN thin layer, and κ_{Si} is the prescribed bending curvature of the Si substrate.

Through equation (4), we now can obtain the equivalent displacement boundary condition from the current large scale bending analysis to the next scale compression analysis.

2.4 Symmetric compression analysis of silicon-nitride and graphene coupled structure

The graphene is prepared by mechanical exfoliation of highly oriented pyrolytic graphite (HOPG). We assume that by Van der Waals forces, the monolayer/multi-layer graphene is closely attached to the smooth surface of the silicon nitride thin layer and covers the hourglass imperfection. Consequently, the deformation near the hourglass imperfection will influence the graphene bifurcation configuration and its localized deformation. We were interested in calculating the simulated graphene slope profile and curvature distribution. The slope difference is one of the key parameters in the quantum-flexoelectric crinkle-analysis model.

The physical dimension of our silicon nitride substrate is 30*30*0.2 (unit: μm). The monolayer graphene thin layer has a dimension of 0.4*0.4*0.0003 (unit: μm). We set the length ratio between the experiment sample and the simulation model equal to 1. Thus, all of the models share the same micron unit from the experiment. To minimize the asymmetry and the computational cost, we build a symmetric geometry model, which is a quarter of the actual sample. The detailed dimensions are shown in Figure (2.16).

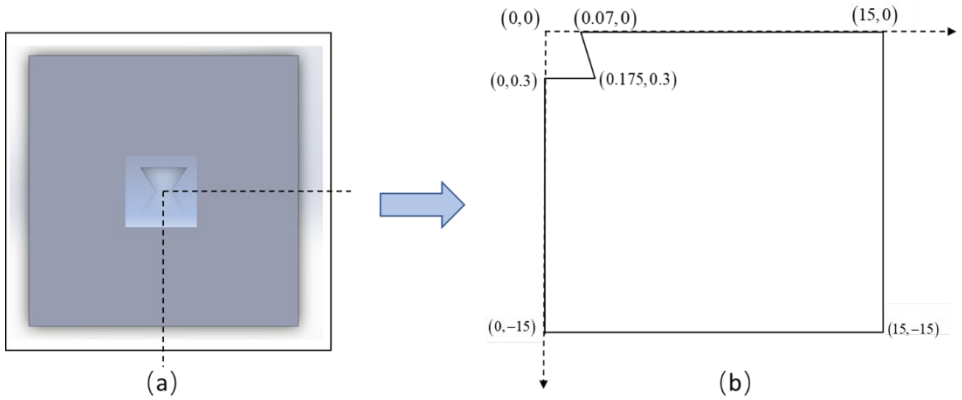

Figure 6.16 Schematics of SiN-graphene coupled structure: (a) the schematic of symmetry analysis; (b) the dimensions of simulation domain.

In the modeling part, we build a 4*4*0.01 graphene thin plate, with Young's modulus 50 Gpa and 0.2 Poisson's ratio. The thin plate is tied with the silicon nitride thin layer and covered the hourglass imperfection. To test the effect of silicon nitride substrate size, we perform simulations with increasing edge length of the substrate. The simulation data are shown in Table 2.1.

Table 2.1 Benchmark test data for substrate size

Size of Si3N4 Substrate	Length ratio L_s/L_g	Maximum and Minimum U3 displacement in graphene
2μm * 2μm*0.2μm	5:1	25nm-7nm
4μm * 4μm*0.2μm	10:1	39nm-11nm
8μm * 8μm*0.2μm	20:1	44nm-15nm
10μm * 10μm*0.2μm	25:1	45nm-16nm

It can be seen the difference between the ten μm length substate and eight μm length substrate is not significant. Thus, we choose 15*15 as our symmetric SiN simulation domain. Note that one of our samples has a dimension of 20*20*0.2, which also means the selected substrate size is appropriate. To mesh the SiN thin layer with finite thickness, we choose 3D solid element. For

graphene, we use a 3D shell element to capture its characteristic thickness. One of the advantages of choosing 3D shell elements is because the shell element can accommodate the high aspect ratio of graphene. The other advantage is the low computational cost and easy modification of the thickness. We have two options for the 3D shell element: the S4 element and the S8R element. According to the ABAQUS document [21], the S8R element are more suitable to a thick plate with a thickness of more than 1/15 of its edge length. Our preliminary test results also show the S8R element more sensitive to the hourglass effect. Thus, we choose the S4 fully integrated elements with second-order accuracy.

Table 2.2 Benchmark test data for mesh size of graphene

Graphene mesh size	U3 maximum displacement
0.012	59nm
0.006	46nm
0.003	41nm
0.0015	40nm

Table (2.2) present the mesh size sensitivity analysis of the S4 element. The U3 maximum displacement difference is less than 1nm when we have a 0.0015 seed size. We also confirmed the mesh sensitivity of silicon nitride substrate. Table (2.3) is the summarized mesh information and material properties of our model.

Table 2.3 Summarized graphene and silicon nitride input data

	Model	Simulation domain size	Young's modulus	Poisson's ratio	Element type	Element number
Si_3N_4	3D Solids	10*10*0.2	160Gpa	0.2	C3D8R	211992
Graphene	3D Shell	0.4*0.4*3e-4	1Tpa	0.3	S4	17689

Figure (2.17) shows the partitioned mesh of the silicon nitride substrate and graphene. The denser mesh is applied in the hourglass neighboring area. In the simulation, the graphene covered the surface over the central imperfection.

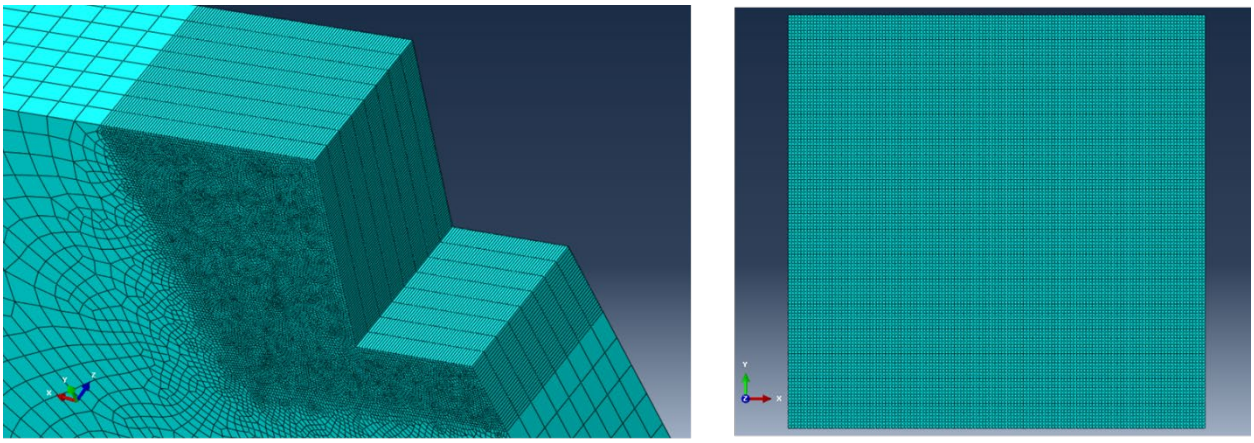

(a) (b)

Figure 2.17 Meshing the SiN-graphene coupled structure: (a) denser mesh near the hourglass hour (b) structured mesh of graphene.

The boundary conditions for the silicon nitride and graphene are set as follow:

Silicon nitride substrate:

Left side edge: U1 = 0.75

Top edge: YSYMM U2 = UR1 =UR3 = 0

Right side edge: XSYMM U1 = UR2 = UR3 = 0

Right bottom corner: U3 = 0

Surfaces normal to X-Y plane: U3 = 0

Graphene:

Top edge: YSYMM U2 = UR1 =UR3 = 0

Right side edge: XSYMM U1 = UR2 = UR3 = 0

Here, the 0.75 µm applied displacement in the SiN layer left side edge is the equivalent strain of 72 m^{-1} bending curvature from the Si substrate bending analysis, given as

$$\frac{0.75}{Q} = 72\ m^{-1} \tag{4}$$

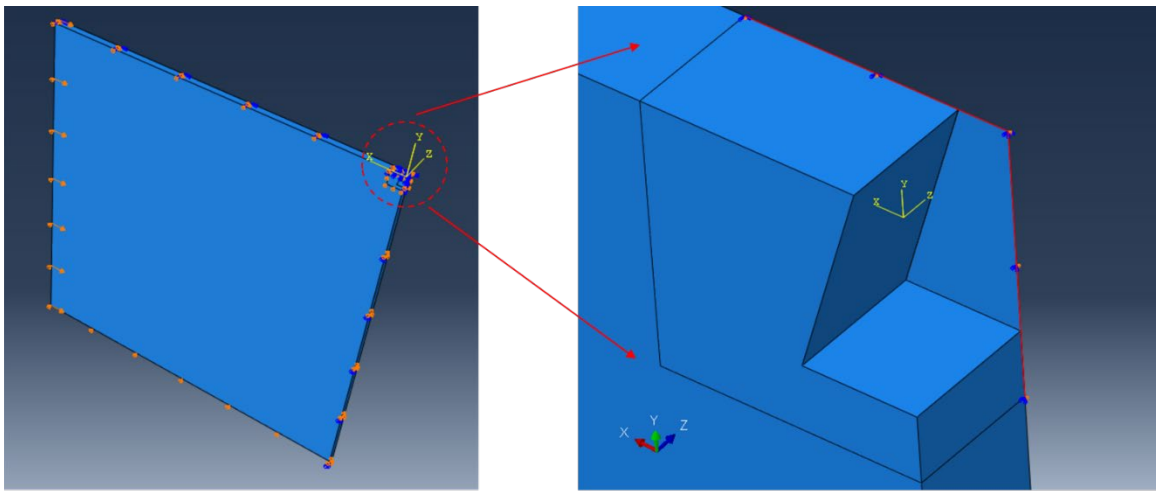

Figure 2.18 Boundary conditions of ¼ SiN layer and graphene thin film.

The final compressed substrate U3 displacement distribution is shown in Figure (2.19). The maximum vertical displacement is 45.3 nm, and it appears both on the tips of the narrow neck of the hourglass hole. The maximum deflection decreases gradually towards the surrounding area, but it becomes a constant in the region contacted with the silicon wafer.

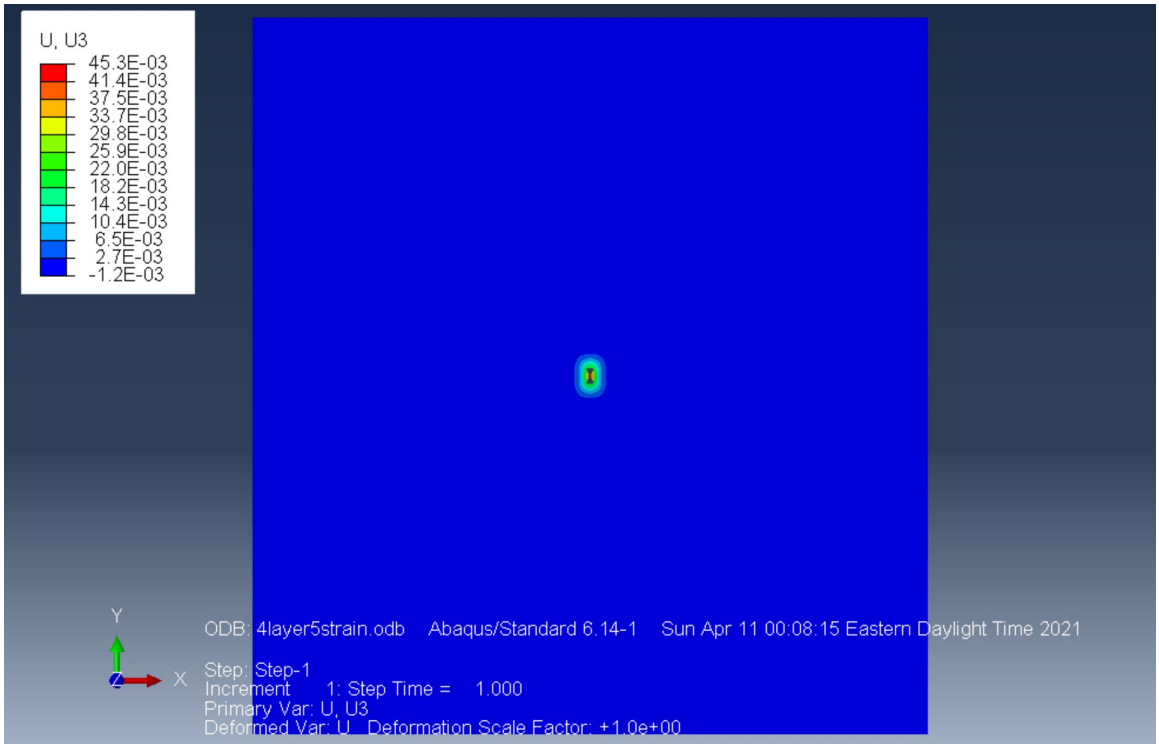

Figure 2.19 Full-field U3 displacement distribution of SiN layer compression analysis.

Figure (2.20) shows the U3 displacement contour of graphene. The central part of graphene bulges above the hourglass hole and the plane of the substrate. Similarly, the maximum U3 displacement is 56.3 nm, and it decreases gradually to the edges of graphene.

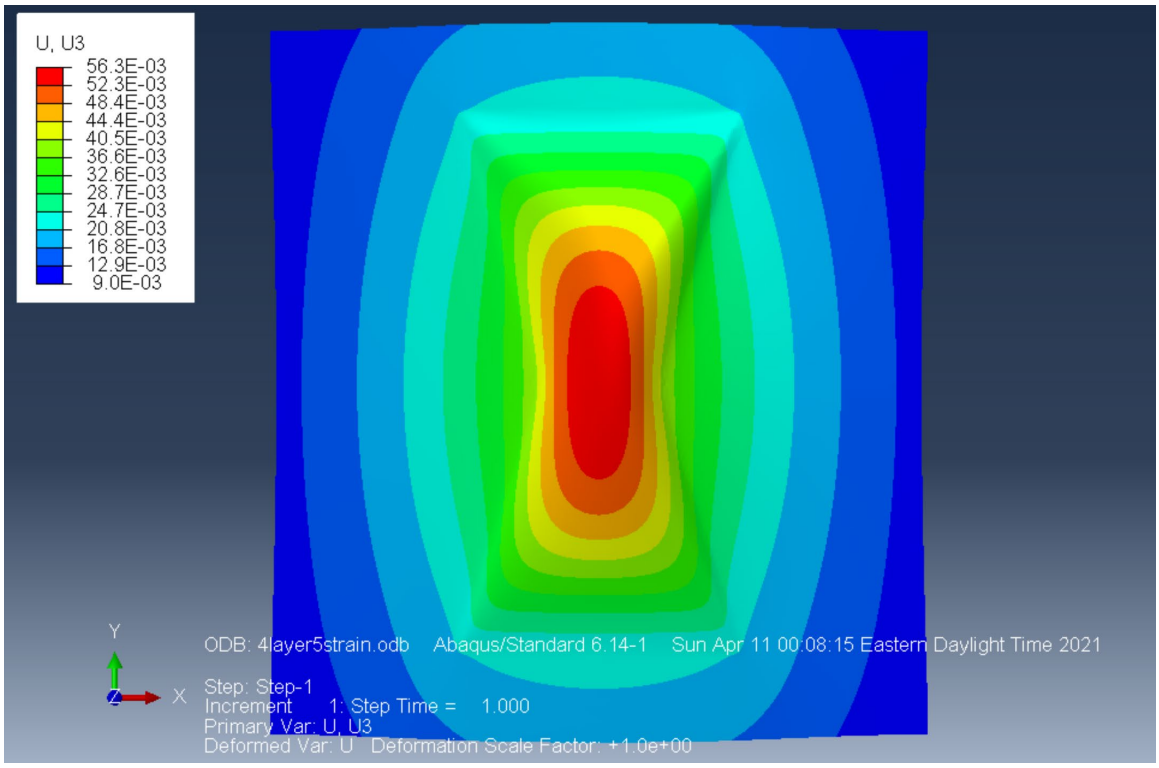

Figure 2.20 Full-field U3 displacement distribution of graphene thin film compression analysis.

The simulated displacement data is not continuous due to the finite mesh size and may result in a high crinkle angle calculation error. Therefore, it is imperative to 2D interpolate the displacement data to obtain the continuous displacement field. According to the ABAQUS manual about shell element formulation [23], the isoparametric S4 element schematic is shown in Figure (2.21).

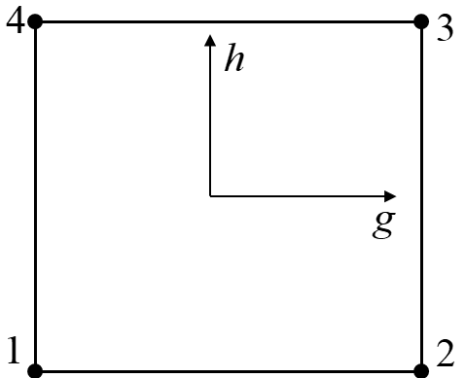

Figure 2.21 The schematic of isoparametric shell element

The shape function of the S4 element as follows [23]:

$$u=\frac{1}{4}(1-g)(1-h)u_1+\frac{1}{4}(1+g)(1-h)u_2+\frac{1}{4}(1+g)(1+h)u_3+\frac{1}{4}(1-g)(1+h)u_4 \tag{5}$$

where g,h are the natural coordinates and $u_1...u_4$ are the displacement data.

Next, we wrote a Python script to extract the displacement data from ODB files and interpolate the data by shape function (5). Finally, the continuous displacement field is obtained.

After we obtained the continuous deformation of silicon nitride and graphene, we approached our final goal of the decomposed finite element simulations: calculating the GEL angle and curvature. The GEL angle distribution of graphene is crucial because it is the critical parameter in length scale-bridging calculations of flexoelectric crinkle angle. There are serval methods to calculate the GEL angle and curvature of graphene. The most effective one is the discrete difference method. Presume we have two data rows, x_{data} are coordinates data for N nodes, and the z_{data} row is relative U3 displacement data.

$$x_{data}=(x_0,x_1,x_2,...,x_n) \tag{6}$$

$$z_{data}=(z_0,z_1,z_2,...,z_n) \tag{7}$$

By the curvature definition, the curvature for a beam is the through-thickness gradient of axial strain. It is also the second derivative of the z-axis direction displacement, i.e., U3 displacement. Equation (8) is the formula to calculate the x-axis direction curvature. We start by calculating the GEL angle, which is the first derivative of the difference between two neighboring U3 data. Then we take one more derivative for calculating the curvature; see Equations (8-10)

$$\kappa_n = \frac{\frac{z_{n+1}-z_n}{x_{n+1}-x_n} - \frac{z_n-z_{n-1}}{x_n-x_{n-1}}}{\frac{x_{n+1}-x_{n-1}}{2}} \quad \text{when } n = 2,3,4,\ldots N-1 \tag{8}$$

For the first and the last data point, we use external linear interpolation:

$$\kappa_1 = \frac{\kappa_2 - \kappa_3}{x_2 - x_3}\left(x_1 - x_2\right) + \kappa_2 \tag{9}$$

$$\kappa_N = \frac{\kappa_{N-1} - \kappa_{N-2}}{x_{N-1} - x_{N-2}}\left(x_N - x_{N-1}\right) + \kappa_{N-1} \tag{10}$$

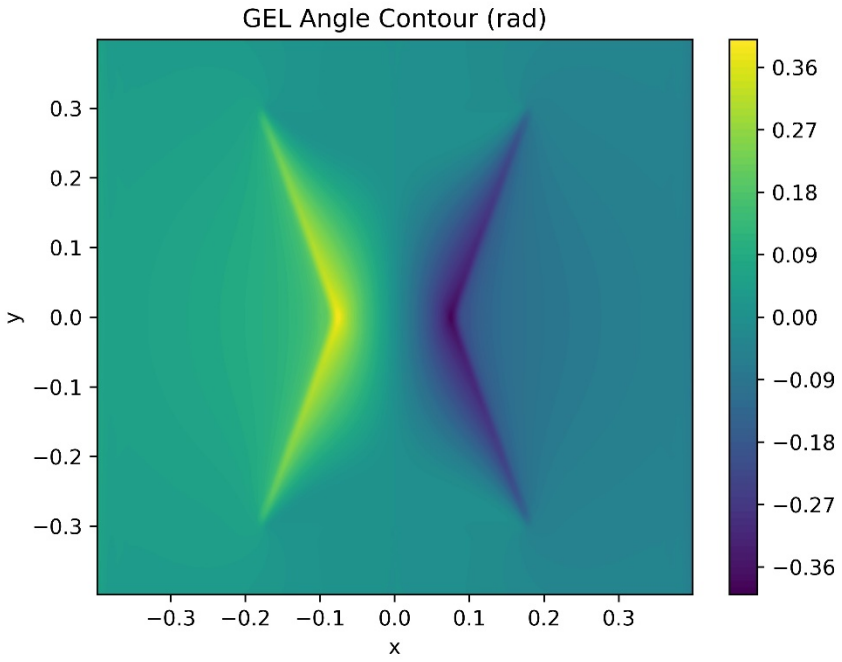

Figure 2.22 Full-field GEL angle distribution of 4 layers graphene under 0.5% applied strain

The calculated GEL graphene angle contour is shown in Figure (2.22). Two kinked bands come out and symmetric about the x-axis. The kinked bands are located along the hourglass hole edge of the silicon nitride substrate. The maximum positive angle appears near the edge of the kinked light-yellow band at the left side, and the minimum negative angle appears near the edge of the kinked dark-blue band at the right. If we look from left to right, the angle varies from a positive to a negative value at the middle of the two kinked bands, which means the curvature reaches the maximum at the middle.

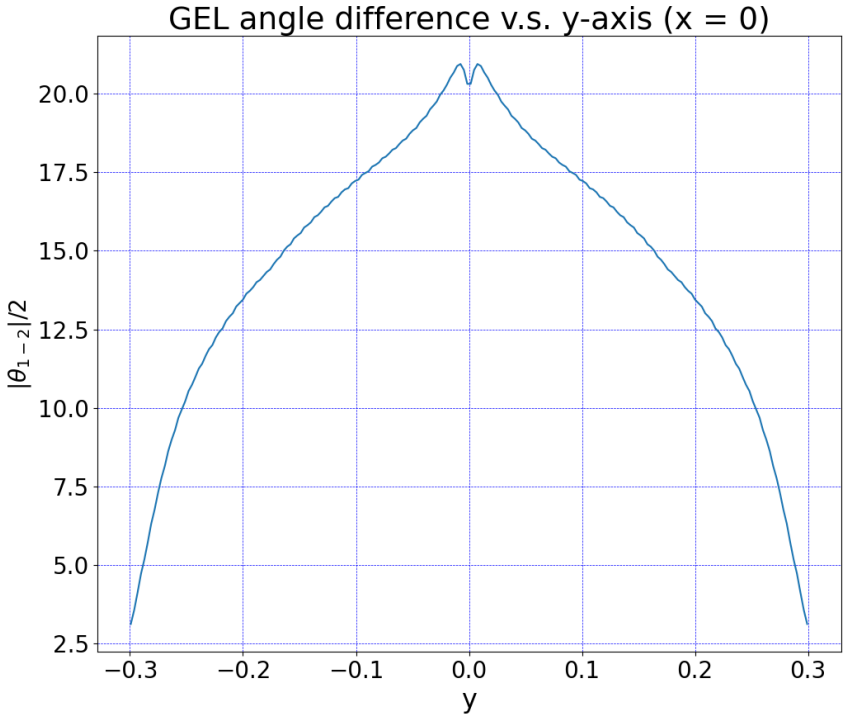

Figure 7.23 GEL slope-angle difference between left and right bands of the hourglass hole of 4 layers graphene under 0.5% applied strain

Figure (2.23) shows the variation along the y direction, of the maximum graphene-slope-angle (in x-direction) difference between the left and the right bands in Fig. 2.22. The maximum angle

difference, 22.2°, is located near, but slightly away from, the center $(x = 0, y = 0)$. The slight deviation of the maximum locations is believed to be due to the sharp kinks at the central boundary $(y = 0)$ of the hourglass hole.

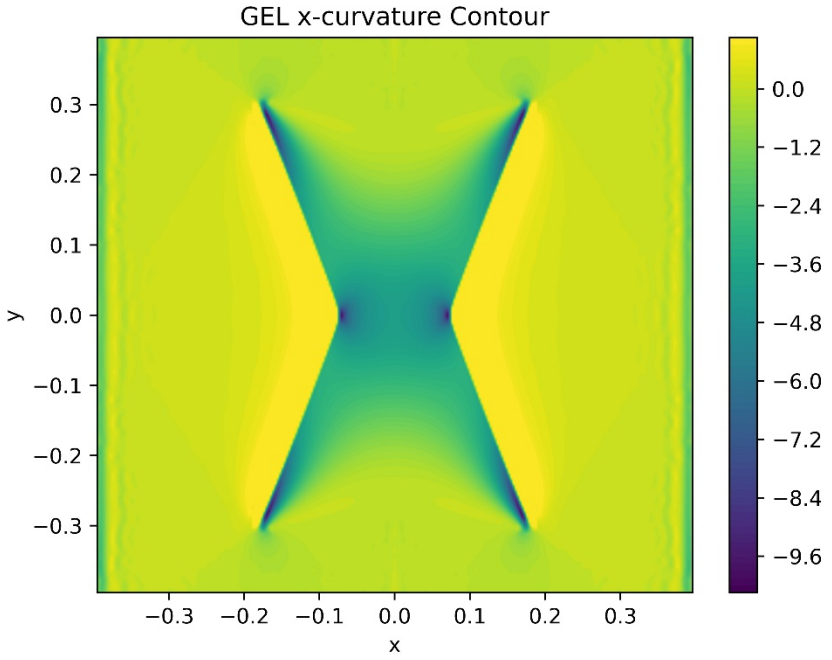

Figure 2.24 Full-field GEL x-curvature distribution of 4 layers graphene under 0.5% applied strain

As we will use partial slope and curvature in x direction, $\frac{\partial u}{\partial x}$ and $\frac{\partial^2 u}{\partial x^2}$, to bridge the FEM results to the quantum-flexoelectric crinkle angles and curvatures in the following section, we denote $\frac{\partial^2 u}{\partial x^2}$ as 'x-curvature' in the rest of this section. In the GEL x-curvature contour (see Figure 2.24), the high concentration of x-curvature along the edges of the hourglass hole is believed to be caused by a single-layer GEL shell-element simulation. However, our interest is in the local-minimum (in x direction) x-curvature zone near the center $(x = 0, y = 0)$ along the y axis $(x = 0)$.

Figure (2.25) shows the absolute curvature distribution along the y-axis direction where$x = 0$. The curvature change in the y direction is symmetric with respect to the center point. From top to bottom, the curvature decreases from zero to a minimum value at $y = 0$ and symmetrically increases thereafter.

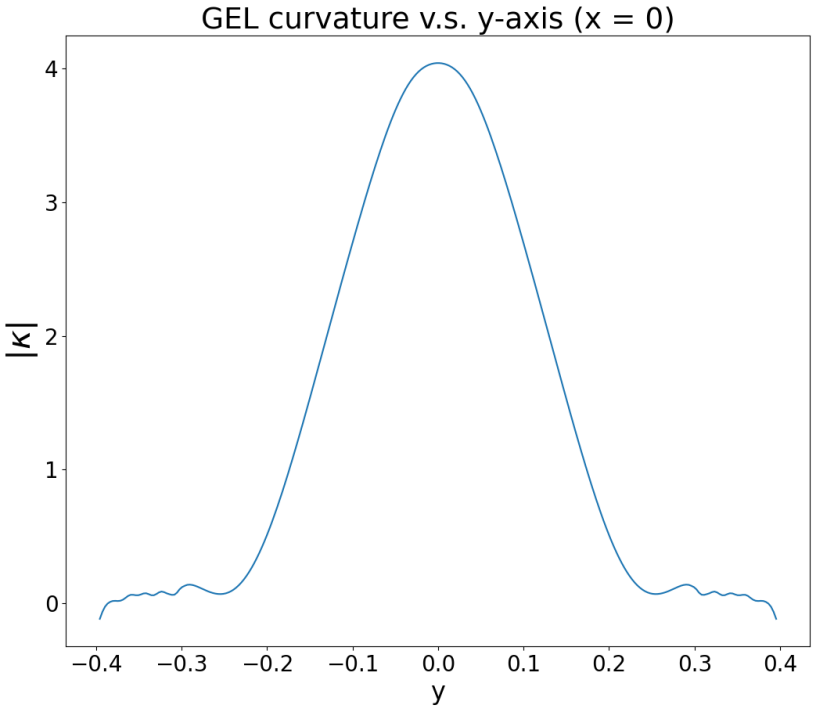

Figure 2.25 Absolute GEL x-curvature distribution along the y-axis of 4 layers graphene with 0.5% applied strain

After we obtained the GEL angle and GEL x-curvature distribution for fixed parameters, such as the thickness of graphene, applied strain rate, it would be interesting to build a non-dimensional model, and analyze the effect of thickness and applied strain variations through a parameter study. Figure (2.26) is the schematic of the graphene and silicon nitride coupled structure.

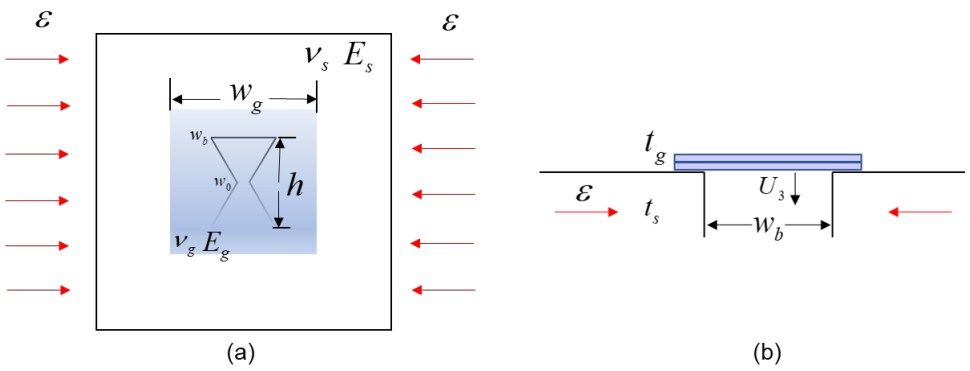

Figure 8.26 Schematics of the compression simulation and specific parameters. (a) Top view of compressing of SiN-graphene assembly; (b) Cross-sectional view of the SiN-graphene assembly.

We have

$$U_3 = f\left(x, y; \boldsymbol{\varepsilon}; E_g, E_s, \nu_g, \nu_s, t_g, t_s, w_b, L, w_0, h, w_g\right) \tag{11}$$

where U_3 is the displacement normal out of the plane, x, y are the coordinates, $\boldsymbol{\varepsilon}$ is the applied strain, E_g, E_s are the Young's modulus, and ν_g, ν_s are Poission's ratios of silicon nitride and graphene respectively, t_g is the multi-layer graphene thickness, t_s is the substrate thickness, h is the height of the hourglass imperfection, w_b is the larger width of the hourglass imperfection, w_0 is the shorter width of the hourglass imperfection, and w_g is the width of GEL.

Nondimensionalized the equation (7), we obtained

$$\frac{U_3}{t_s} = f\left(\frac{x}{t_s}, \frac{y}{t_s}; \boldsymbol{\varepsilon}; \frac{E_g}{E_s}, \nu_g, \nu_s, \frac{t_g}{t_s}, \frac{w_b}{t_s}, \frac{L}{t_s}, \frac{w_0}{t_s}, \frac{h}{t_s}, \frac{w_g}{t_s}\right) \tag{12}$$

Our interests are the variations of $\frac{t_g}{t_s}, \boldsymbol{\varepsilon}$. Thus we have

$$\frac{U_3}{t_s} = \overline{f}\left(\boldsymbol{\xi}, \eta; \boldsymbol{\varepsilon}; \frac{t_g}{t_s}\right) \tag{13}$$

where $\xi = \frac{x}{t_s}, \eta = \frac{y}{t_s}$

Figure (2.27) presents the linear relation between the increasing applied strain and the central normalized deflection. The strain test results indicate applied strain must not exceed

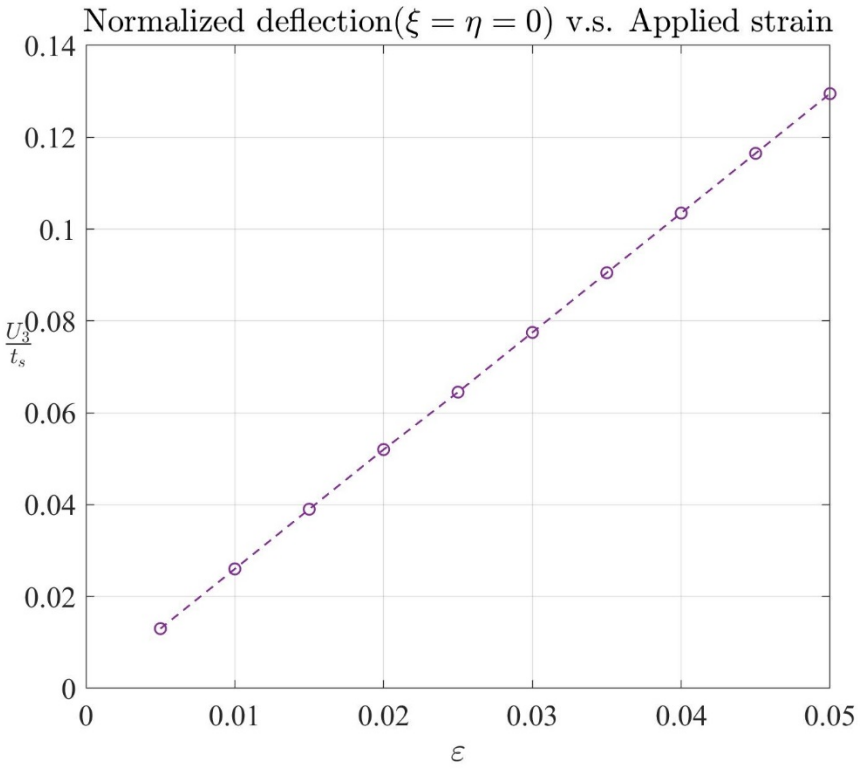

Figure 2.27 Relationship between normalized central deflection and the applied strain.

the threshold value 5%; otherwise, the narrow hourglass neck vertex in the silicon nitride substrate will contact and break the sample.

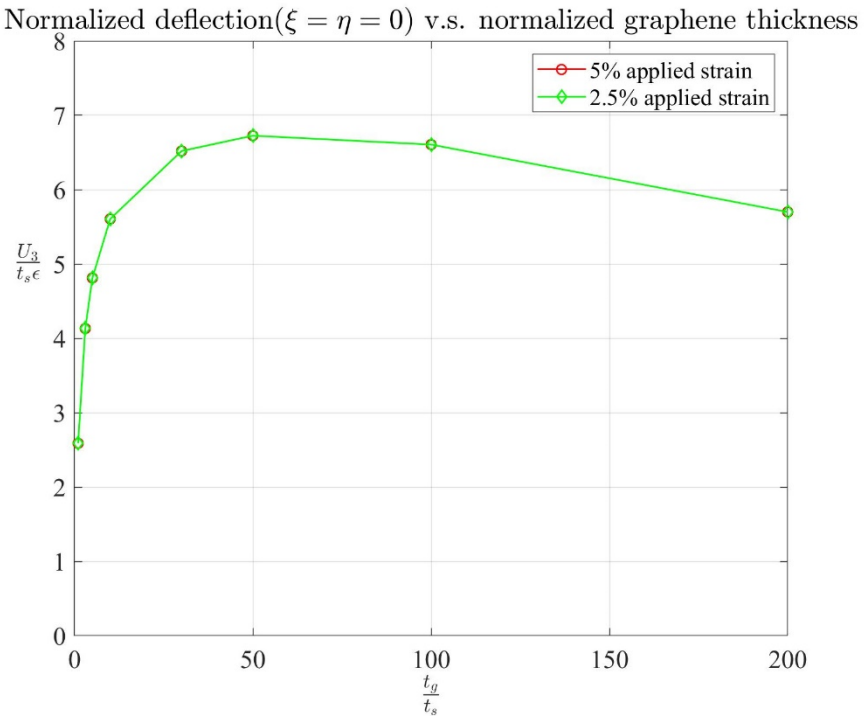

Figure 2.28 Relationship between the central normalized deflection and the normalized graphene thickness.

In Figure (2.28), we plot the effect of increasing normalized graphene thickness with respect to the normalized central deflection under different applied strains. Two curves merged because of the specified non-dimensional form of the deflection. In the initial stage, the deflection will increase along within 50 normalized graphene thickness. However, the normalized central deflection decrease if the normalized graphene thickness exceeds the threshold value. We explain the reverse is due to the change of the graphene's bending stiffness. In the beginning, the few layers of graphene have low bending stiffness, which makes substrate deformation dominants. When the bending stiffness of multi-layer graphene increased to the threshold value, graphene with high bending stiffness becomes the essential part to resist the bending moment and therefore reduce the deflection.

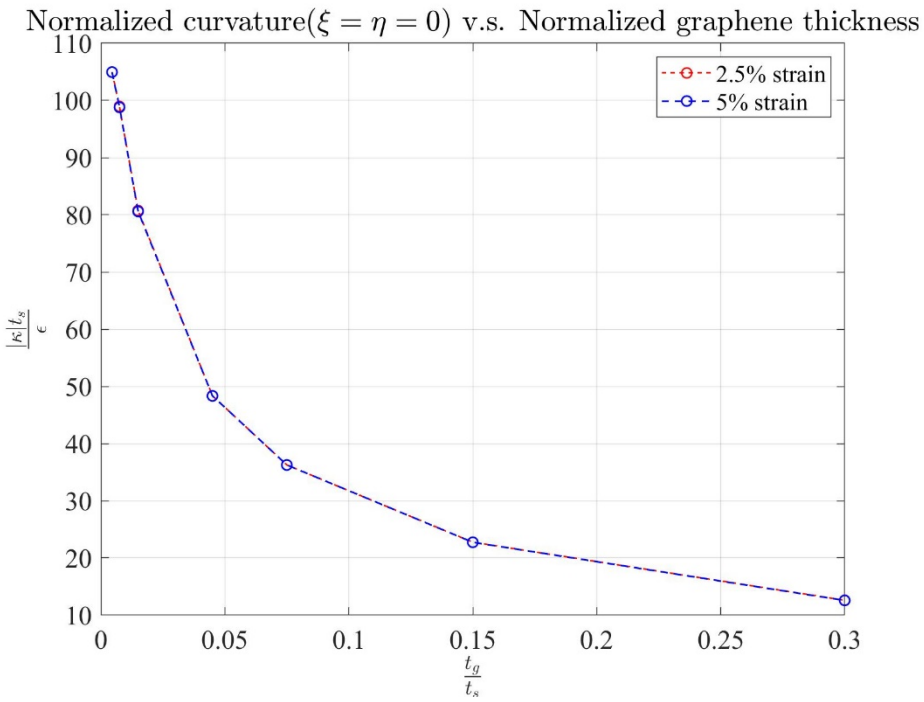

Figure 2.29 Relationship between the central normalized deflection and the normalized central x-curvature.

Figure (2.29) shows the normalized central curvature change with different normalized graphene thicknesses. A larger normalized thickness will yield smaller normalized curvature in the center. Unlike the normalized deflection curve, there is no reverse curvature change. This inconsistency between the trend of deflection and the curvature is due to the change of buckling configuration. The larger graphene thickness causes the minimum curvature from the central line $y = 0$ to move to the lateral edges.

Chapter 3: Computational length scale-bridging calculation of quantum crinkle angle

3.1 Scale-bridging technique and assumptions

Typically, there is a considerable length gap between the hand on experiments and the nanoscale mechanics phenomena. In this thesis project, the length scale of the experiment sample is 1e-3 m, while the length scale for graphene crinkle is 1e-9 m. A key question raised: how could we predict the nanoscale behavior of graphene crinkle from the continuum scale experiment and simulation? The solution for this question is the Scale-bridging technique, which provides us the way to connect the mesoscale with the nanoscale problem. The scale-bridging technique plays a fundamental role in multiscale research fields [24-28]. With the help of the scale bridging technique, the Finite element simulation can be coupled with molecular dynamics simulations. Moreover, the simulation domain is extended from the coarse to quantum with less computational cost [29].

Before applying the scale-bridging technique to graphene crinkle, we quickly review the current experimental and computational research results of graphene crinkle. Li *et al.* [8] report the new experimental discovery of kinked corrugation in multi-layer graphene. Kothari *et al.* [15] further explored the condition of graphene deformation from wrinkle mode to crinkle mode. The DFT calculation indicates the curvature localization typically within the 2 nm wide boundary layer. To understand the crinkle forming mechanism, they modeled the multi-layer elastic graphene layers with weak Van der Waals coupling as the pure mechanical sandwich structure. By using the energy method, the critical buckling load for this structure is obtained. Note that for the sandwich structure model, the total energy only includes the bending energies, as well as the interlayer shearing. By contrast with DFT results, the mechanical sandwich model predicts the progressive curvature localization cover a 50–100 nm wide boundary layer. The reason for the inconsistency is the

quantum flexoelectricity effect in graphene. The localized curvature breaks the equilibrium of the electron cloud distribution in the graphene. The polarization density entered a nonequilibrium state and made the crinkle tip be able to release the positive and negative electric charge. This electric charge is also the key traction force for fixing the DNA molecular chain in the experiment. They also built the quantum flexoelectric graphene crinkle analysis model and revealed the dipole-dipole interaction at the nanoscale when crinkle forming.

To correctly apply the length scale bridging technique, serval important assumptions need to be made. First, we assume multi-layer graphene is pure elastic isotropic materials with the symmetry angle and length distribution in the lateral direction. Second, we assume the coupled interaction between the layers of graphene is the bending moment coupled with the interlayer shearing. When the multi-layer graphene under applied strain, we assume each layer deforms identically in the thickness direction.

3.2 Flexoelectric crinkle angle calculation

With the help of the crinkle analysis framework [17], we can bridge our finite element simulation result from a large scale to a quantum scale. In the finite element analysis, we are modeling the graphene with isotropic elastic material as a rectangular Kirchhoff-Love plate.

As the post-buckling process is in a supercritical state with gentle load variation (less than 0.4% variation), we would like to match the reaction force (the post-buckling load) between graphene and the SiN film to the FEM buckling load. The mechanical buckling load of N-layer MLG is ~0.2% higher than flexoelectric buckling load, and we will match the mechanical buckling load to get the equivalent layer number:

$$f_{cr} = \mu\left(N-1\right)a + \frac{\pi^2 Q_b N}{4L_0^2} = \frac{\pi^2 EI}{4L_0^2\left(1-\nu^2\right)} \tag{14}$$

where f_{cr} is the critical buckling load for multi-layer graphene and N is the scale bridged layer number of graphene, $\boldsymbol{\mu}$ is the DFT calculated interlayer shear modulus and Q_b is the bending stiffness of each layer. L_0 is the average bandwidth. a is the interlayer spacing. E is the Young's modulus of graphene, v denote the Poisson's ratio of graphene, I is the area moment of inertia of the thin graphene plate in the FE model.

The two terms in the left side of equation (10) are the critical load evaluated in the interlayer shearing graphene buckling model, and the right side part is the theoretical buckling load of our FEM. It can scale up the FE graphene thickness to the equivalent graphene layer number in the proposed graphene crinkle model. Giving an arbitrary graphene layer number, we set up the equivalent thickness in our FE model, Vice versa, See Figure (3.1)

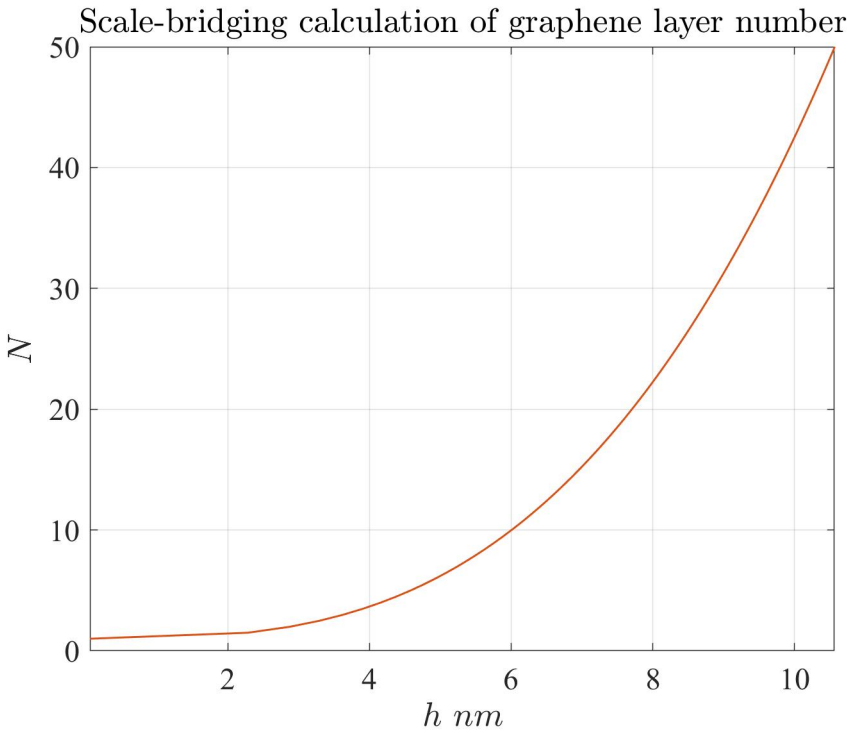

Figure 3.1 Relationship between the equivalent experimental graphene thin film layer number with GEL thickness in FE model.

In the next part of this chapter, we begin to calculate the graphene crinkle angle based on the FE simulation.

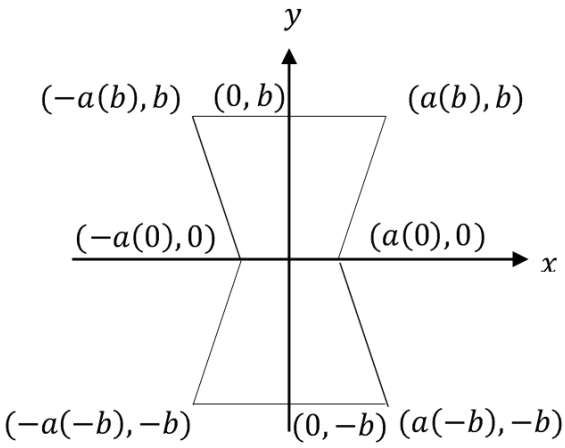

Figure 3.2 Schematic of the hourglass shape and the nodal coordinates.

Figure (3.2) present the GEL angle contour and key point coordinates on the graphene surface. We set up the kinked edge as the function a of y-axis coordinates. The height of the hourglass shape is $2b$. From the FE simulation, we obtained the curved buckling configuration with varied slope angles. We would like to match the length of the sine-wave shape of simulated graphene post-buckling shape with the length of the saw-tooth crinkle shape, finally to calculate the equivalent graphene crinkle.

Therefore, we have

$$a(y)\sqrt{\left(\theta_{crinkle}(y)\right)^2+1} \approx \frac{1}{2}\int_{-a(y)}^{a(y)} \sqrt{1+\theta^2}\,dx \tag{15}$$

where the left term denotes the approximate crinkle roof slope length, the right term is the integral form of graphene curve length. $\theta_{crinkle}(y)$ is the scale-bridged crinkle angle, and θ is the FE GEL angle align with the x-axis. Then, the angle for graphene crinkle along the y axis is given as

$$\theta_{crinkle}(y) \approx \sqrt{\left\{ \frac{1}{2a(y)} \int_{-a(y)}^{a(y)} \sqrt{1+\theta^2}\, dx \right\}^2 - 1} \tag{16}$$

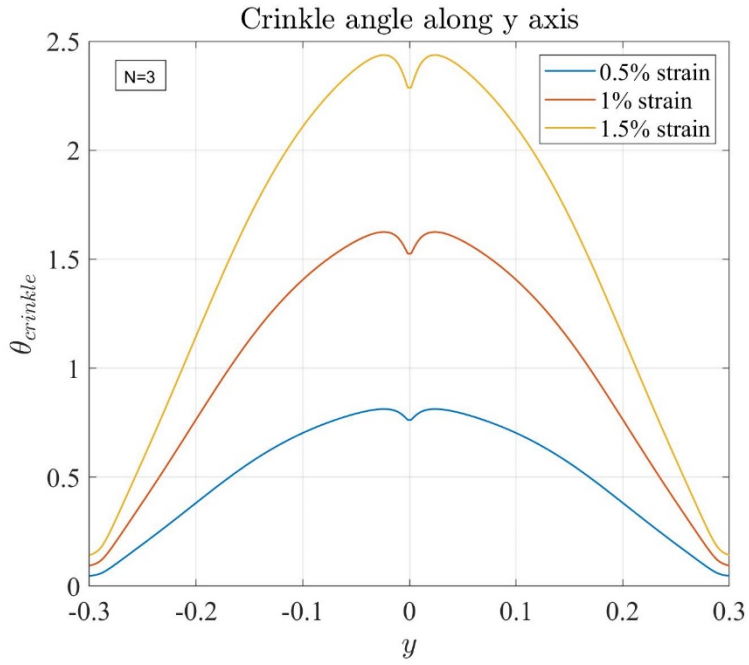

Figure 3.3 Flexoelectric crinkle angle distribution along y-axis when three layers graphene under different strain.

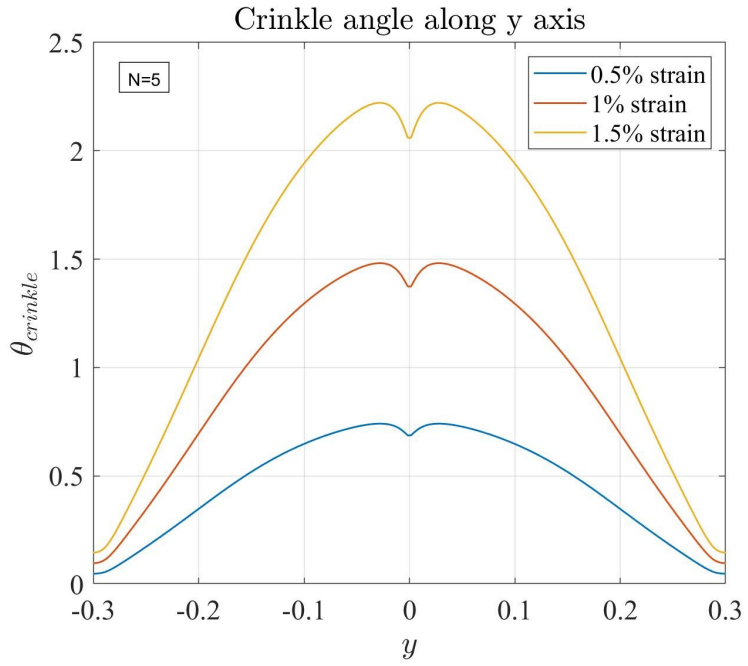

Figure 3.4 Flexoelectric crinkle angle distribution along y-axis when five layers graphene under different strain

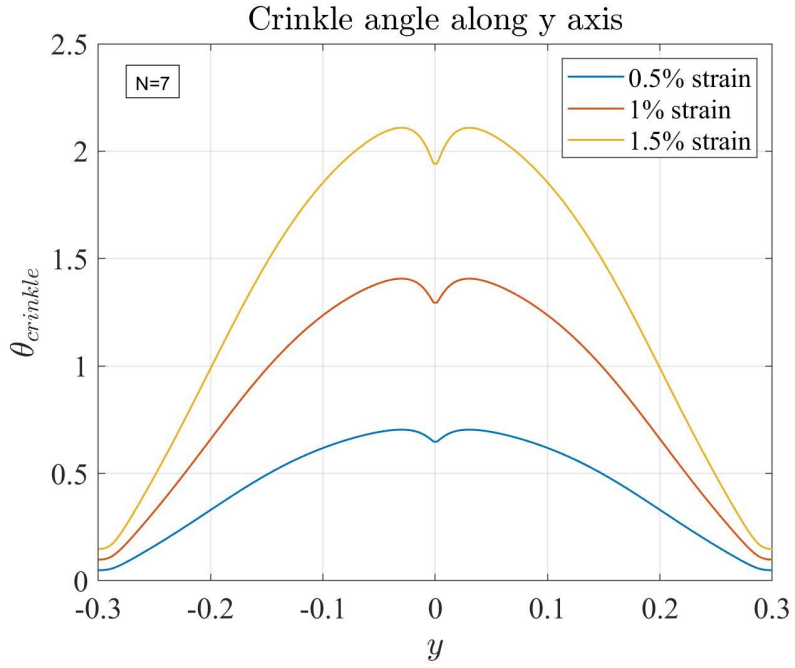

Figure 3.5 Flexoelectric crinkle angle distribution along y-axis when seven layers graphene under different strain

Figure (3.3-3.5) shown us the scale-bridged graphene crinkle angle distributions for three layers, five layers, seven layers graphene, respectively. It can be seen the higher applied strain leads larger crinkle angle, and the crinkle angle decreases with larger layer numbers of graphene. It is due to the increase of multi-layer graphene bending stiffness, and the buckling load is significantly increased with the larger interlayer resistance. It is also worth note that the graphene crinkle angle has the local minimum in the top/bottom edges of the hourglass shape (i.e.,$y = \pm 0.3$). Ideally, the crinkle angle in the top/bottom edges should vanish to zero because of the fixed boundary conditions [15]. Here, we attribute the non-zero crinkle angle due to the nitride substrate coupled deformation. From the previous DFT analysis [15], one of the essential features of the multi-layer graphene crinkle is the reversed curvature outside of the curvature localization band. It is also confirmed in these figures. Besides, two reverses are observed near the localized maximum crinkle angle (i.e., where $y = 0$). Two local maximum crinkle angle appears where $y = \pm 0.03$. We explain this intriguing phenomenon as the high strain concentration in the narrow neck of the hourglass hole in the substrate. It's been observed that the vertexes of the hourglass narrow neck bulge out of the surrounding substrate surface, which may influence the crinkle angle at the same position.

Chapter 4: Conclusions and discussion

We summarize the important conclusions in this thesis as follow:

1. Our finite element analysis predicts the multi-layer graphene will bulge out of the plane of silicon nitride thin sheet, and the maximum deflection concentrate in the center of the hourglass shape hole.
2. The response parameter $Q = 0.0103\ \mu m/m^{-1}$ is presented as the critical scale-bridging parameter from the bending analysis of Si wafer to compression of SiN-graphene coupled structure.
3. During the graphene buckling process, the hourglass hole caused the symmetry graphene angle distribution, the maximum positive/negative rotation angle and positive curvature appear in both kinked lateral edges of the hourglass shape. Along the y-axis direction, curvature first increases from zero to the maximum then vanishes to zero. The maximum x-axis direction angle difference is also found in the narrow neck part.
4. In the non-dimensional analysis, the normalized maximum deflection increases with the small graphene thickness while decrease with the larger graphene thickness. However, the normalized central curvature is monotonically decreasing with the increase of graphene thickness.
5. Our scale-bridging calculation shows that a larger applied strain leads to a higher flexoelectric crinkle angle along the y axis. The increase of graphene layer number reduces the flexoelectric crinkle angle localization.

There are still spaces for optimizing the finite element analysis. For example, we only assume all materials are linear elastic, and isotropic. It can be replaced by user-defined anisotropic materials.

Next, the interface interactions between the silicon wafer substrate and the silicon nitride thin film can be taken into consideration. It would be more accurate to model the tie interaction between the silicon nitride thin film and the graphene as the cohesive zone. Then, the influence of the substrate on graphene could be more accurate. In the future, we will consider these potential improvements to make the simulation more effective.

References

[1] J. A. Rogers, T. Someya, Y. Huang, Materials and mechanics for stretchable electronics. Science 327, 1603-1607 (2010).

[2] Nagashima, So, et al. "Tunable nanochannels fabricated by mechanical wrinkling/folding of a stiff skin on a soft polymer." Advanced Materials Interfaces 2.3 (2015): 1400493.

[3] Novoselov, Kostya S., et al. "Electric field effect in atomically thin carbon films." science 306.5696 (2004): 666-669.

[4] Zhang, Qiangqiang, et al. "3D printing of graphene aerogels." Small 12.13 (2016): 1702-1708.

[5] Kitipornchai, S., X. Q. He, and K. M. Liew. "Continuum model for the vibration of multilayered graphene sheets." Physical Review B 72.7 (2005): 075443.

[6] Liu, Lincong, et al. "Recent advances in friction and lubrication of graphene and other 2D materials: Mechanisms and applications." Friction 7.3 (2019): 199-216.

[7] Zhong, Lei, Huajian Gao, and Xiaoyan Li. "Atomistic simulations of the tensile behavior of graphene fibers." Extreme Mechanics Letters 37 (2020): 100699.

[8] Li, Ruizhi, et al. "A new subcritical nanostructure of graphene—Crinkle-Ruga structure and its novel properties." MRS Advances 3.45-46 (2018): 2763-2769.

[9] Wang, Yitao, and Zhaoxu Meng. "Mechanical and Viscoelastic Properties of Wrinkled Graphene Reinforced Polymer Nanocomposites–Effect of Interlayer Sliding within Graphene Sheets." Carbon (2021).

[10] Hu, Haixiao, et al. "Experimental and numerical investigations of wrinkle effect on failure behavior of curved composite laminates." Composite Structures 261 (2021): 113541.

[11] Huang, Wei, et al. "Wrinkling analysis of circular membranes by a Fourier based reduced model." Thin-Walled Structures 161 (2021): 107512.

[12] Hu, Hengqian, et al. "Eliminating graphene wrinkles by strain engineering." Extreme Mechanics Letters 42 (2021): 101104.

[13] Varillas, Javier, and Otakar Frank. "Wrinkle development in graphene sheets with patterned nano-protrusions: A molecular dynamics study." Carbon 173 (2021): 301-310.

[14] Zhong, Lei, Huajian Gao, and Xiaoyan Li. "Atomistic simulations of the tensile behavior of graphene fibers." Extreme Mechanics Letters 37 (2020): 100699.

[15] Zhang, Teng, Xiaoyan Li, and Huajian Gao. "Designing graphene structures with controlled distributions of topological defects: A case study of toughness enhancement in graphene ruga." Extreme Mechanics Letters 1 (2014): 3-8.

[16] Meyer, Jannik C. "A. k. Geim, MI Katsnelson, KS Novoselov, TJ Booth and S. Roth." Nature 446 (2007): 60-63.

[17] Kothari, Mrityunjay, Moon-Hyun Cha, and Kyung-Suk Kim. "Critical curvature localization in graphene. I. Quantum-flexoelectricity effect." Proceedings of the Royal Society A: Mathematical, Physical and Engineering Sciences 474.2214 (2018): 20180054.

[18] Holley, Robert W., et al. "Structure of a ribonucleic acid." Science (1965): 1462-1465.

[19] Sanger, Fred, and Alan R. Coulson. "A rapid method for determining sequences in DNA by primed synthesis with DNA polymerase." Journal of molecular biology 94.3 (1975): 441-448.

[20] Margulies, Marcel, et al. "Genome sequencing in microfabricated high-density picolitre reactors." Nature 437.7057 (2005): 376-380.

[21] Greenleaf, William J., and Arend Sidow. "The future of sequencing: convergence of intelligent design and market Darwinism." (2014): 1-3.

[22] Clarke, James, et al. "Continuous base identification for single-molecule nanopore DNA sequencing." Nature nanotechnology 4.4 (2009): 265-270.

[23] ABAQUS Inc, (2006). Finite-strain shell element formulation. https://classes.engineering.wustl.edu/2009/spring/mase5513/abaqus/docs/v6.6/books/stm/default.htm?startat=ch03s06ath83.html#stm-elm-finitestrainshells

[24] Krajewski, Paul E., et al. "Microstructure-based multiscale modeling of elevated temperature deformation in aluminum alloys." Acta Materialia 58.3 (2010): 1074-1086.

[25] Mehar, Kulmani, and Subrata Kumar Panda. "Multiscale modeling approach for thermal buckling analysis of nanocomposite curved structure." Advances in nano research 7.3 (2019): 181.

[26] Srivastava, A., et al. "A multiscale approach to modeling formability of dual-phase steels." Modelling and Simulation in Materials Science and Engineering 24.2 (2016): 025011.

[27] Keralavarma, S. M., A. F. Bower, and W. A. Curtin. "Quantum-to-continuum prediction of ductility loss in aluminium–magnesium alloys due to dynamic strain aging." Nature communications 5.1 (2014): 1-8.

[28] Li, Xikui, and Ke Wan. "A bridging scale method for granular materials with discrete particle assembly–Cosserat continuum modeling." Computers and Geotechnics 38.8 (2011): 1052-1068.

[29] Wagner, Gregory J., and Wing Kam Liu. "Coupling of atomistic and continuum simulations using a bridging scale decomposition." Journal of Computational Physics 190.1 (2003): 249-274.

Appendix A